



A review of the simulation studies on the bulk growth of silicon carbide single crystals

Minh-Tan Ha¹ · Seong-Min Jeong¹

Received: 9 November 2021 / Revised: 6 January 2022 / Accepted: 13 January 2022 / Published online: 18 February 2022
© The Korean Ceramic Society 2022

Abstract

Silicon carbide (SiC) is a wide-bandgap semiconductor material that is viable for the next generation of high-performance and high-power electrical devices. In general, bulk SiC single crystals have been grown at very high temperatures in a closed reactor; hence, the growth process is difficult to monitor using in situ techniques. Consequently, computational simulations have been utilized to understand, validate, and design crystal growth processes. In this review, we summarize the results of computational simulations of SiC bulk crystal growth using three primary methods: physical vapor transport, high-temperature chemical vapor deposition, and top-seeded solution growth. The simulations reveal the effects of physicochemical phenomena, such as temperature distribution, fluid flow, and chemical reactions, on crystal growth behaviors. Process parameters for high-quality and high-yield crystal growth have been realized with the aid of simulations. Furthermore, recent advances in machine learning techniques for accelerating the design of crystal growth parameters and enabling real-time parameter optimization are introduced. Overall, computational simulations are a crucial tool for the development of SiC bulk crystal growth and its applications.

Keywords Silicon carbide · SiC · Crystal growth · Simulation · Process design

List of symbols

H	Magnetic field intensity, A/m
B	Magnetic flux density, T
A	Magnetic potential vector, Vs/m
ω	Angular frequency, rad/s
E	Electric field intensity, V/m
D	Electric flux density, C/m ²
J	Electric current density, A/m ²
σ	Electrical conductivity, S/m
i	Imaginary unit
Re	Real part of a complex number
Q	Heat, J
ρ	Density, kg/m ³
C_p	Heat capacity, J/(kg·K)
T	Temperature, K
k	Thermal conductivity, W/(m·K)
G	Surface irradiation, W/m ²
G_m	Mutual surface irradiation, W/m ²
F_{amb}	Ambient view factor

ϵ_s	Surface emissivity
σ_{sb}	Stefan–Boltzmann constant, W/(m ² K ⁴)
T_{amb}	Ambient temperature, K
J	Surface radiosity, W/m ²
n	Radiation direction vector
u	Velocity field, m/s
p	Pressure, Pa
t	Time, s
τ	Viscous stress, Pa
F_{ext}	External force density, N/m ³
D	Diffusion coefficient, m ² /s
c	Concentration, mol/m ³
G_{rate}	Growth rate, m/s
M	Molar mass, g/mol
$J_{species}$	Mass flux, mol/m ² s
r	Radius, m
S	Area, m ²
K	Equilibrium constant
P	Partial pressure, Pa
R	Molar gas constant, J/molK
S_{eff}	Effective vapor supersaturation
A	Pre-exponential factor

✉ Seong-Min Jeong
smjeong@kicet.re.kr

¹ Semiconductor Materials Center, Korea Institute of Ceramic Engineering and Technology, Jinju 52851, South Korea

1 Introduction

Silicon carbide (SiC) is a wide bandgap semiconductor that is a candidate for replacing Si substrates for high-power electronic devices [1–6]. Since Acheson first synthesized SiC in 1891 [7], SiC has been synthesized or fabricated using various methods. Although SiC has more than 200 polytypes [8, 9], the 4H-SiC and 6H-SiC polytypes are thought to be suitable for single-crystal substrates because of their optimal bandgap, thermal conductivity, and breakdown voltage [3–5, 10, 11].

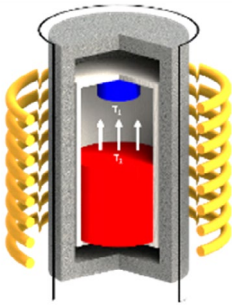
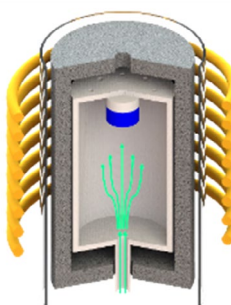
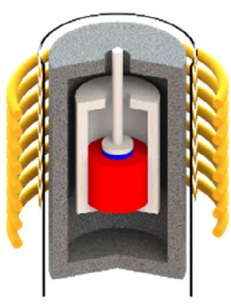
In this review, we focus on crystal growth methods that can mass-produce commercial-grade SiC substrates: physical vapor transport (PVT), high-temperature chemical vapor deposition (HTCVD), and top-seeded solution growth (TSSG). A brief summary of each method, including a schematic, the source materials, the growth rate, and the processing temperature, are listed in Table 1.

The PVT method, also known as the sublimation–recrystallization method or the modified Lely method, was introduced by Tairov and Tsvetkov in 1978 [19]. Currently, most commercial SiC wafers are fabricated using the PVT method [22]. In the PVT method, the starting material is typically SiC powder with a relatively large particle size (> 200 μm). Under atmospheric pressure, SiC sublimates to numerous vapor species (Si, C, Si₂C,

SiC₂, and SiC) at a very high temperature (2830 °C) [5]. Under the low-pressure conditions (typically a few torr) in the PVT reactor, SiC starts to sublime below 2000 °C. The composition of the vapor species is thermodynamically determined by the temperature and pressure inside the reactor. The temperature gradient between the source material and the seed is the driving force for the transport of vapor species from the source surface to the seed surface in the reactor. Subsequently, the transported vapor species recrystallize on the seed, contributing to bulk crystal growth.

In 1996, Kordina et al. introduced the HTCVD method to grow SiC single crystals [20]. The significant advantage of HTCVD for SiC crystal growth is its high growth rate, which is up to 2.4 mm/h in recent reports [14, 15]. In this method, the starting materials are gas-phase sources. When monosilane (SiH₄) is adopted as the Si source, hydrocarbons (such as C₃H₈ or CH₄) are used as the C source. Typically, Ar, He, and H₂ are used as carrier gases. Furthermore, H₂ plays an important role in controlling the C/H and Si/H ratios of the vapor species. Single-source materials containing both Si and C, such as tetramethylsilane (TMS) and methyltrichlorosilane (MTS), have also been proposed as the starting materials for HTCVD growth of SiC bulk crystals [23–34]. At the very high temperatures in HTCVD reactors, the introduced gas sources decompose into Si_xC_y and other vapor species. The flow rate of the starting gases is

Table 1 Summary of methods for growing SiC bulk crystals [12–18]

	PVT	HTCVD	TSSG
Schematic			
Source materials	SiC powder	SiH ₄ , SiCl ₄ , TMS, C ₃ H ₈ , CH ₄ , C ₂ H ₂ , ...	Si + metals flux Carbon
Developed in	1978 (Tairov, Russia) [19]	1996 (Kordina, Sweden) [20]	1999 (Hofmann, Germany) [21]
Size	6 inches (150 mm) / Commercialized	4 inches (100 mm) / Commercialized	4 inches (100 mm) / Developing
Growth rate	200 ~ 400 $\mu\text{m}/\text{h}$ 2 mm/h (max)	0.6 ~ 1.2 mm/h 2.4 mm/h (max)	0.4 ~ 1.0 mm/h 2 mm/h (max)
Temperature	2100 ~ 2500 °C	2200 ~ 2500 °C	1700 ~ 2200 °C

controlled to obtain an appropriate C/Si ratio of the Si_xC_y vapor species. Similar to the PVT method, the Si_xC_y vapor species are transported to and deposited on the seed crystal, which is located at the top of the reactor.

In 1999, Hofmann et al. reported the liquid-phase crystal growth of SiC single crystals based on the TSSG technique [21]. High-quality SiC single crystals can be achieved under the quasi-equilibrium growing conditions of the TSSG method [35, 36]. In contrast to the PVT and HTCVD methods, in which the crystallization occurs at the vapor/solid interface, SiC crystals grow at the liquid/solid interface in the TSSG method. The liquid is a Si melt containing dissolved C at a temperature typically between 1700 and 2000 °C, which is substantially lower than the process temperatures in the PVT and HTCVD methods. Note that C powder is not used as the C source in TSSG to avoid the incorporation of C powder in the grown SiC crystal. Instead, C is supplied from the graphite crucible containing the Si melt. C dissolves from the crucible walls into the Si melt, then diffusively and convectively travels to the seed surface and contributes to crystal growth. Therefore, the graphite crucible simultaneously acts as a reservoir for the Si melt and the C source in the TSSG method, which enables continuous C supply in the Si–C melt during SiC growth.

Because SiC crystal growth methods are typically conducted at very high temperatures in induction furnaces, in situ investigation inside the growth cells covered by graphite insulators is nearly unfeasible. The growth cell for SiC is known as a “black box,” in which the phenomena inside are invisible. Consequently, simulations have provided further understanding of the physicochemical behaviors of the crystal growth system and accelerated process optimization for SiC bulk crystal growth. Therefore, this review aims to summarize the efforts to simulate and optimize the bulk SiC single-crystal growth process and the prospective direction of simulations for SiC crystal growth.

Because there is a wide range of numerical and thermodynamic simulation approaches, common simulations that share the underlying physics between growth methods are presented in the second section. The third section provides simulation-based advanced analysis and process optimization for the major challenges of each crystal growth method. In the PVT method, the optimal design of the temperature distribution in the reactor is crucial for determining the vapor composition, growth rate, and crystal quality. The key issues in the HTCVD method are determining the dependence of the vapor species ratio on temperature and pressure and producing an optimal hot-zone design that maintains a stable flow of the vapor species under the quasi-equilibrium state to grow high-quality SiC crystals. In the TSSG method, increasing the C solubility and transport effectiveness in the melt is a critical challenge for enhancing the growth rate and crystal quality. In the fourth section, recent advances in machine learning for

real-time supervision and optimization of SiC crystal growth are presented with applications for the TSSG method.

2 Common simulations for SiC bulk crystal growth

This section describes the theoretical basis of the physics of SiC growth, which is used for the simulations. Because SiC crystals are grown at very high temperatures, typically in induction furnaces, the simulation of SiC crystal growth first considers the induction heating problem by employing the electromagnetic field generated by the induction coils and heat transfer in the solid, liquid, and vapor phases. The mass transport of dilute species (vapor or liquid phase) in growth cell media (vapor, liquid, and porous) is considered. Simulating crystal growth involves numerically solving a series of partial differential equations (PDEs) governing various multiphysics phenomena in the crystal growth system. Numerical analysis methods, such as the finite volume method (FVM) or finite-element method (FEM), are generally adopted to solve these multiphysics equations.

First, the electromagnetic field generated by the induction coil is calculated by deriving and solving Maxwell's equations:

$$\nabla \times \mathbf{H} = \mathbf{J} \quad (1)$$

$$\mathbf{B} = \nabla \times \mathbf{A} \quad (2)$$

$$\mathbf{E} = -i\omega\mathbf{A} \quad (3)$$

$$\mathbf{J} = \sigma\mathbf{E} + i\omega\mathbf{D} \quad (4)$$

Then, the heat Q is given as the resistive losses Q_r and magnetic losses Q_m :

$$\begin{aligned} Q &= Q_r + Q_m \\ &= 0.5\text{Re}(\mathbf{J} \cdot \mathbf{E}) + 0.5\text{Re}(i\omega\mathbf{B} \cdot \mathbf{H}). \end{aligned} \quad (5)$$

The heat transfer via thermal conduction is calculated by

$$\rho C_p \cdot \nabla T = \nabla \cdot (k\nabla T) + Q \quad (6)$$

Because crystal growth is performed at high temperatures, the heat transfer by radiation must be considered. The heat transfer by radiation is calculated by the following equations:

$$G = G_m(J) + F_{\text{amb}}\sigma_{\text{sb}}T_{\text{amb}}^4 \quad (7)$$

$$(1 - \varepsilon_s)G = J - \varepsilon_s\sigma_{\text{sb}}T^4 \quad (8)$$

$$\varepsilon_s(G - \sigma_{\text{sb}}T^4) = -\mathbf{n} \cdot (-k\nabla T) \quad (9)$$

In crystal growth, the transport of the vapor or liquid phase is an important step that governs the growth rate and

crystal quality. Therefore, the mass transport of the vapor or liquid phase is the primary task to be explored by simulations. The fluid flow is mathematically expressed by the Navier–Stokes and conservation equations (Eqs. 10–11, respectively), the mass transport of the vapor or liquid phase is driven by the convection and diffusion of the fluid (Eq. 12), and the species flux toward the seed crystal defines the growth rate (Eq. 13):

$$\rho \left(\frac{\partial \mathbf{u}}{\partial t} + \mathbf{u} \cdot \nabla \mathbf{u} \right) = \nabla \cdot [-p + \boldsymbol{\tau}] + \mathbf{F}_{\text{ext}} \quad (10)$$

$$\nabla \cdot \mathbf{u} = 0 \quad (11)$$

$$\nabla \cdot (-D \nabla c) + \mathbf{u} \cdot \nabla c = 0 \quad (12)$$

$$G_{\text{rate}} = \frac{M_{\text{SiC}}}{\rho \pi r^2} \iint_S J_{\text{species}} dS \quad (13)$$

Based on the Gibbs energy minimization technique in thermodynamic modeling, it is possible to obtain the ratio of chemical species for different temperatures and pressures in the PVT or HTCVD systems [37]. Thermodynamic modeling is also useful for estimating the solubility of C in the multi-component melt in TSSG [38]. In the next section, a further review of the use of simulations for understanding the physicochemical behaviors and for process optimization of the growth methods is discussed.

3 Simulation-based process optimization for SiC crystal growth

3.1 Physical vapor transport

As mentioned in the introduction section, the temperature gradient is the driving force for vapor species transport and crystal growth in the PVT method. Simulations by Chen et al. showed that increasing the induction power causes the global temperature to increase, as shown in Fig. 1a [39]. Moreover, when the temperature gradient between the seed and the powder was fixed, the growth rate increased as the seed temperature increased. In addition, the growth rate increased as the temperature gradient increased when the seed temperature was fixed, as shown in Fig. 1b. Hence, increasing the temperature gradient has been proven to be critical for enhancing the growth rate in the PVT method.

The effects of the thermal properties of the source powder and crucible on the temperature distribution in the PVT method were numerically evaluated. In the late 1990s, Makarov and Karpov et al. developed codes based on the FVM to simulate the temperature distribution and mass transport in PVT systems [40–43]. Figure 2a shows

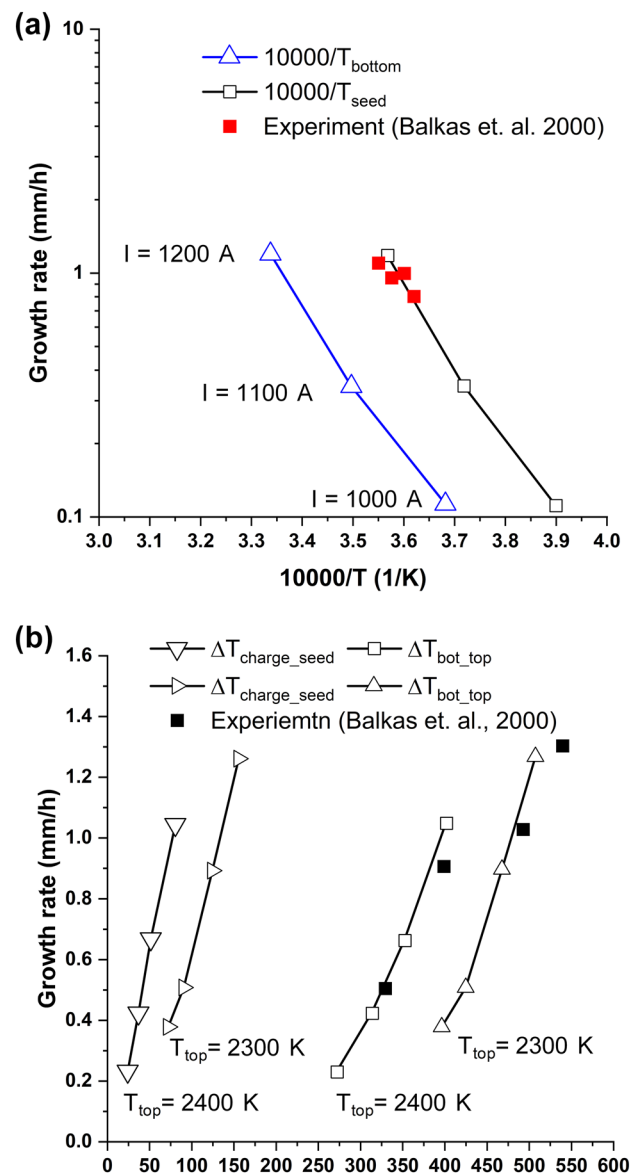


Fig. 1 Dependence of the growth rate on the a seed temperature and b temperature gradient between the seed and the powder [39]

the temperature distributions in the PVT reactor with two types of SiC sources: a polycrystalline block and powder [41]. The thermal conductivity of the SiC powder was 1–2 orders of magnitude smaller than that of the polycrystalline SiC, resulting in a higher vertical temperature gradient for the SiC powder source (Fig. 2b). Hence, SiC powder is preferred for high crystal growth rates.

Steiner et al. calculated the temperature distributions with different thermal conductivities corresponding to various crucible materials and demonstrated that the temperature gradients are less sensitive to the crucible materials, as depicted in Fig. 2c [44].

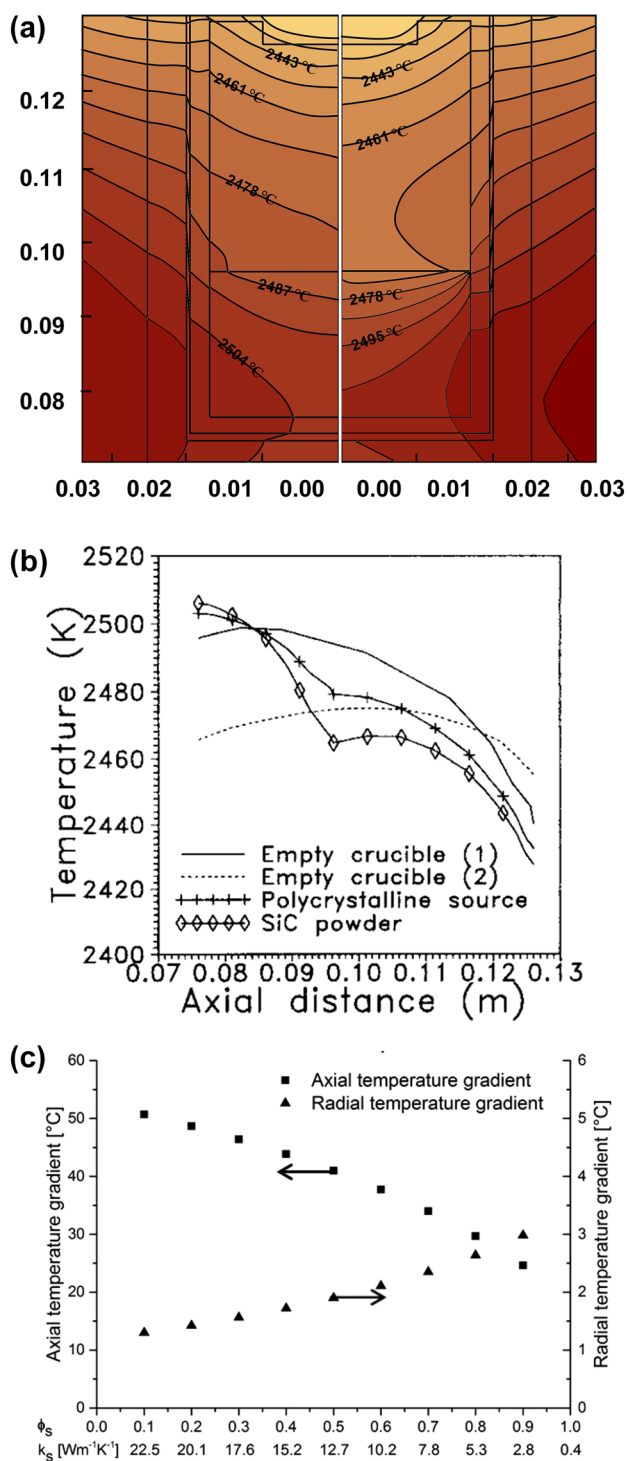
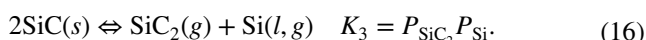
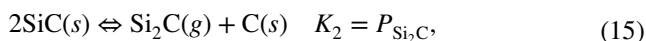
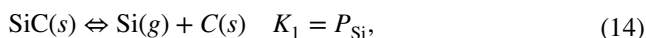


Fig. 2 Temperature distributions with two different SiC sources: **a** polycrystalline SiC block and **b** SiC powder [41]. **c** Variation in the axial and radial temperature gradients in the reactor with the porosity of the SiC powder [44]

Furthermore, modifying the crucible structure is another approach to enhance the temperature gradient and growth rate. Yan et al. proposed using a graphite block inside the crucible (Fig. 3a), which restrains the growth rate at the edge

of the crystal and results in a grown crystal with a convex shape, as shown in Fig. 3b [45].

Another topic in PVT growth is understanding the thermodynamics, kinetics, and transport behaviors of the chemical species in the system. The major vapor species in the PVT method were experimentally identified to be Si, Si₂C, and SiC₂; the fraction of the other species is negligible [46]. Some reactions (Eqs. 14–16) have been proposed for sublimation [39, 47]:



The equilibrium constant K is calculated using Eq. 17, in which the Gibbs energy (ΔG_T^0) is evaluated using the standard heat of formation and the standard enthalpy of the reacting species. Furthermore, the mass balance equation (Eq. 18) was considered [48]:

$$K = \exp(-\Delta G_T^0/RT) \quad (17)$$

$$P_{\text{Si}} + 2P_{\text{Si}_2\text{C}} + P_{\text{SiC}_2} = P_{\text{Si}_2\text{C}} + 2P_{\text{SiC}_2} \quad (18)$$

Karpov et al. calculated the variation in the partial pressure of species with temperature under C-rich (SiC–C) and Si-rich (SiC–Si) conditions, as shown in Fig. 4a, b. These results agree well with experimental data, suggesting that C-rich and Si-rich equilibria co-exist in the system [40]. At the graphite wall, the vapor species–C(s)–SiC(s) three-phase equilibrium is dominated, corresponding to a C-rich equilibrium. At the seed surface, the vapor species–Si(l)–SiC(s) three-phase equilibrium is dominated, corresponding to a Si-rich equilibrium.

Ariyawong et al. showed that the equilibrium is dependent on the temperature gradient and pressure, as shown in Fig. 4c [48]. At a certain temperature, the Si content is enriched when the temperature increases or the total pressure decreases [48, 49]. Moreover, the partial pressures of species are higher under a Si-rich equilibrium, which is favorable for SiC growth. Therefore, increasing the temperature gradient and decreasing the working pressure are mandatory for the fast growth of SiC bulk crystals. Nakamura et al. adopted a TaC-coated graphite crucible, which prevented C sublimation from the crucible and hence increased the Si content to exceed the equilibrium value, resulting in Si inclusions in the grown crystal, as shown in Fig. 4d [50]. These Si inclusions were the origin of micropipes [51], which were the killing defects in SiC-based devices [52]. Furthermore, Tupitsyn et al. observed that when the effective vapor supersaturation (S_{eff} , Eq. 19) was high (3.8 at 2300 °C), and the Si(g)/C(g)

Fig. 3 **a** Schematic of a PVT reactor with graphite blocks attached to the graphite wall. **b** Growth rate at the edge of the crystal decreased, resulting in a convex-shaped crystal [45]

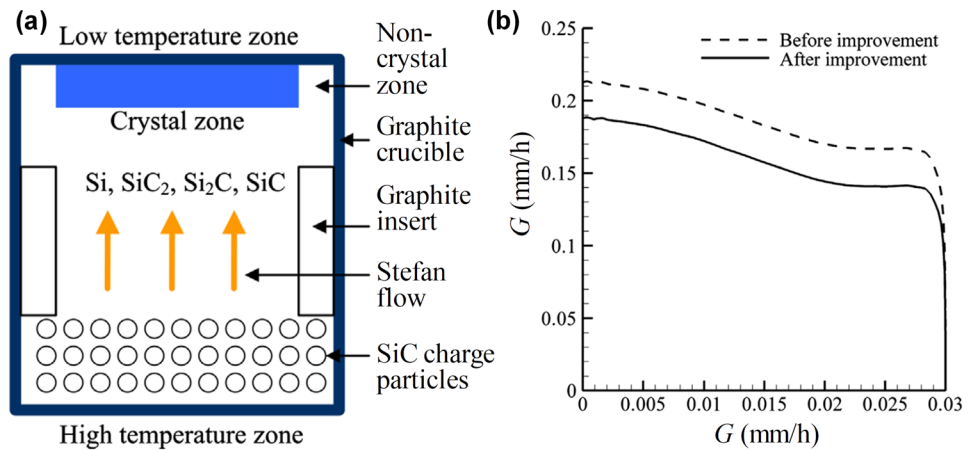
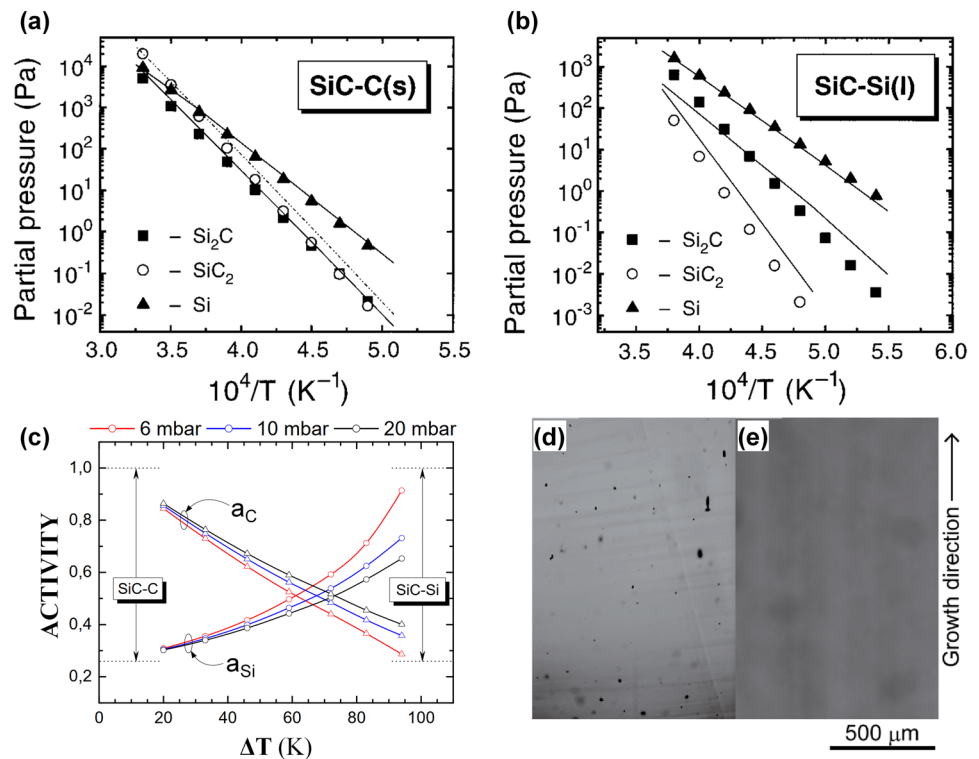


Fig. 4 Partial pressures of Si, Si₂C, and SiC₂ species vs. temperature calculated for three-phase equilibria: **a** SiC–C(s) and **b** SiC–Si(l) [40]. The symbols are experimental points measured for the Si–C system under C-rich (SiC–C) and Si-rich (SiC–Si) conditions [46]. **c** Fractions of C and Si at different pressures vs. temperature [48]. Optical microscopy images of crystal growth with **d** TaC-coated graphite and **e** graphite crucibles [50]



ratio was low (~ 1.3), the 4H polytype was selectively grown, even when the seed was the 6H polytype [53]. Hence, it is clear that the Si/C ratio in the vapor plays an important role in SiC bulk crystal growth:

$$S_{\text{eff}} = (P_{\text{Si}_2\text{C}}^{\text{source}} + 2P_{\text{SiC}_2}^{\text{source}}) / (P_{\text{Si}_2\text{C}}^{\text{seed}} + 2P_{\text{SiC}_2}^{\text{seed}}) \quad (19)$$

Because multiple equilibria coexist in Si–C systems, C-rich or Si-rich vapors are localized at the SiC powder, resulting in the crystallization and graphitization of the SiC source. These behaviors significantly influence crystal growth. As shown in Fig. 5a, graphitization occurs at the

corners of the source powder and the crucible, whereas crystallization occurs at the top of the powder [54]. Crystallization and graphitization cause the stoichiometry, porosity, and thermal properties of the source powder to vary over time. Hence, the temperature distribution and species transport behavior in the PVT reactor are time-dependent. Understanding the evolution of the source powder is crucial for long term and stable growth of SiC bulk crystals.

Kulik et al. proposed a model that describes the graphitization of the powder [55]. The powder was considered to be a porous medium with porosity ϵ and mean particle radius r , as illustrated in Fig. 5b. The vapor species, including Si,

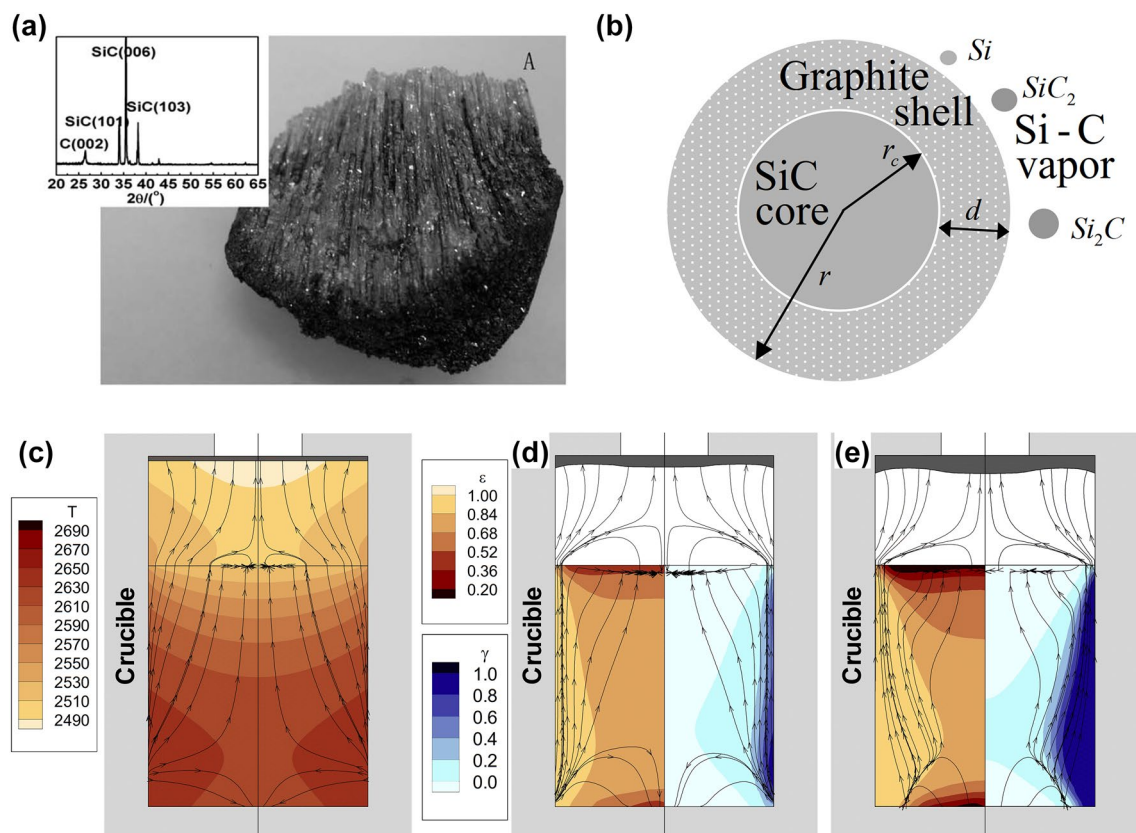


Fig. 5 **a** Crystallization and graphitization of SiC powder [54]. **b** Model for the graphitization of a SiC particle. **c** Streamlines and temperature distribution in a PVT reactor at the beginning of growth.

Streamlines, porosity (ϵ , left side), and graphitization degree (γ , right side) after **d** 10 h and **e** 20 h of growth [55]

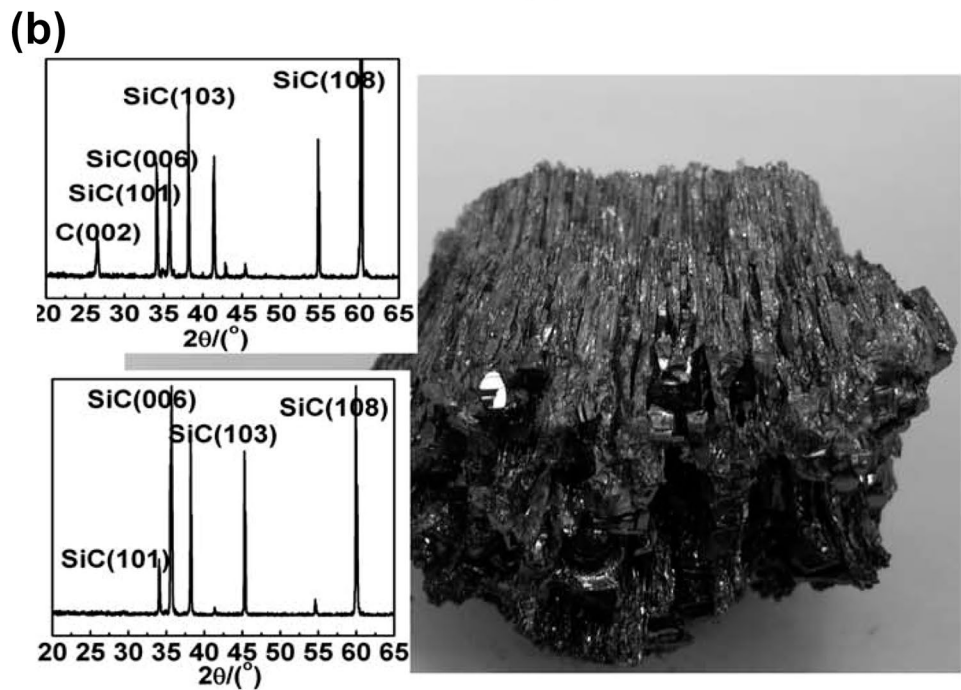
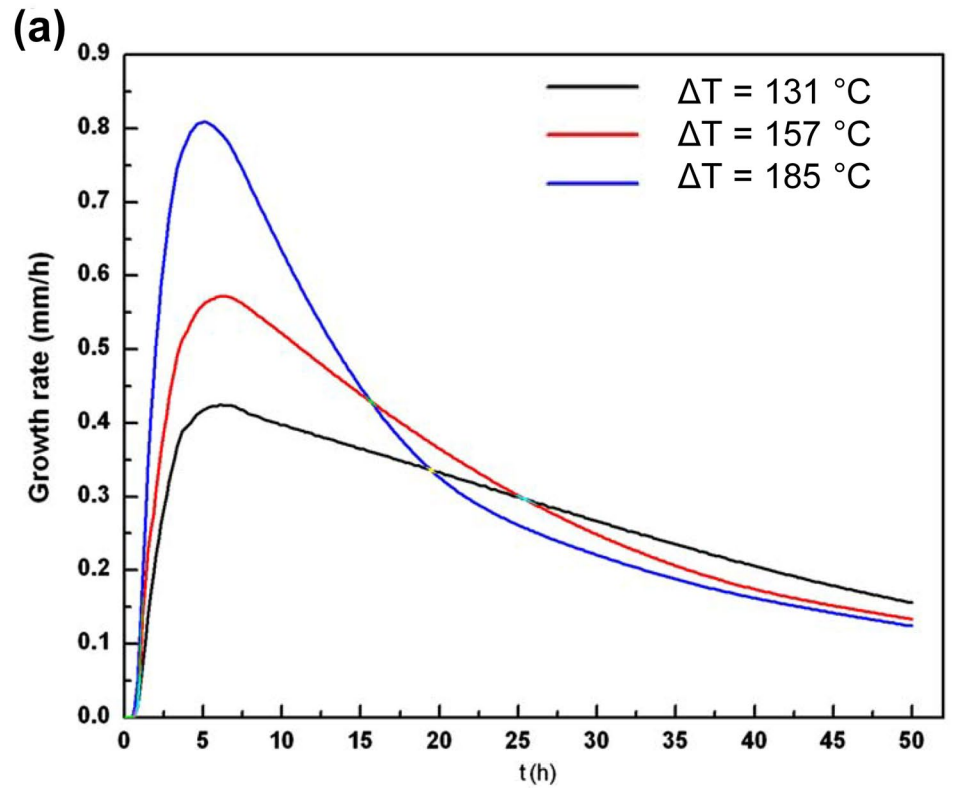
SiC_2 , and Si_2C , were in equilibrium with the graphite shell and SiC core. As the SiC core radius (r_c) decreased, the graphite shell thickness (d) increased owing to the sublimation of SiC. The vapor transport in the powder was calculated using Darcy's law, which describes the flow of a fluid through a porous medium considering the vapor viscosity and powder permeability. Vapor transport in the porous medium of the SiC powder resulted in the formation of channels in the source powder, as shown in Fig. 5a. The channels in the source residue correspond to the temperature streamlines illustrated in Fig. 5c. The temperature streamlines, porosity (ϵ), and graphitization ($\gamma = 1 - (r_c/r)^3$) of the powders after 10 and 20 h are presented in Fig. 5d, e, respectively. The initial porosity was 0.8, and the initial graphitization was 0. The porosity was inversely proportional to crystallization. Moreover, the streamlines preferred to move through the more porous areas, that is, near the wall, increasing the growth rate at the edge of the crystal, whereas the growth rate at the center of the crystal decreased, forming a grown crystal with a concave surface.

Liu et al. showed that crystallization and graphitization affect the growth rate by conducting experiments and simulations of the growth rate over time including the

crystallization and graphitization phenomena [54]. As shown in Fig. 6a, at the early stage of crystal growth, the growth rate was high because of the high temperature gradient and vapor species transport. A high growth rate led to higher degrees of crystallization and graphitization of the powder, resulting in a decrease in the growth rate over time. In an extreme case, where the temperature difference between the seed and the powder was as high as 185 °C, notable crystallization occurred at the bottom of the powder, as shown in Fig. 6b, preventing vapor transport and crystal growth.

Although a high vertical temperature gradient in the PVT reactor enhances the growth rate, it also causes large thermal stress, which induces more dislocations in the crystal. Hence, the temperature gradient should be controlled to obtain high-quality crystals at a reasonable growth rate. The thermal stress of SiC crystal ingots has been calculated [56–59] employing Hooke's law (Eq. 20), in which σ_{**} is the stress component, ϵ_{**} is the strain component, c_{ij} is the elastic coefficient, and α_{\perp} and α_{\parallel} are the thermal expansion coefficients perpendicular and parallel to the c -axis of the SiC crystal, respectively. The strain components are calculated using Eq. 21, where u and v are the axial and radial components of the displacement field, respectively:

Fig. 6 **a** Calculated growth rate over time for different vertical temperature gradients but the same seed temperature. **b** Remained powder for the case of large temperature gradient [54]



$$\begin{pmatrix} \sigma_{rr} \\ \sigma_{\varphi\varphi} \\ \sigma_{zz} \\ \sigma_{rz} \end{pmatrix} = \begin{pmatrix} c_{11} & c_{12} & c_{13} & 0 \\ c_{12} & c_{22} & c_{23} & 0 \\ c_{13} & c_{23} & c_{33} & 0 \\ 0 & 0 & 0 & c_{44} \end{pmatrix} \begin{pmatrix} \epsilon_{rr} - \alpha_{\perp}(T - T_{\text{ref}}) \\ \epsilon_{\varphi\varphi} - \alpha_{\perp}(T - T_{\text{ref}}) \\ \epsilon_{zz} - \alpha_{\parallel}(T - T_{\text{ref}}) \\ \epsilon_{rz} \end{pmatrix} \quad (20)$$

$$\epsilon_{zz} = \frac{\partial u}{\partial z}; \epsilon_{rr} = \frac{\partial v}{\partial z}; \epsilon_{\varphi\varphi} = \frac{v}{r}; \epsilon_{zz} = \frac{\partial v}{\partial z} + \frac{\partial u}{\partial r} \quad (21)$$

In addition, attaching the seed to the crucible lid substantially influences the thermal stress distribution [56, 57]. Figure 7 shows the calculated stress component (σ_{rz}) and the dimensionless dislocation density (N_d) with the crystal attached to the seed holder in different configurations. The dislocation density can be estimated by the difference between the shear stress and critical shear stress in the slip direction [60]. For SiC crystal growth, it is slip on the (0001) plane in the $[11\bar{2}0]$ direction. When the seed was firmly attached to the holder, the stress and dislocation density were high at the rim of the crystal, as shown in Fig. 7a. When the crystal was allowed to displace in the radial direction, as shown in Fig. 7b, the stress and dislocation density located at the shoulder were an order of magnitude smaller than those in the first case. When the crystal was allowed to displace in both the vertical and horizontal directions, the stress and dislocation density decreased, except at the edge of the crystal boule.

The simulation studies confirmed that temperature distribution optimization is crucial in the PVT method. It affects the equilibrium of the vapor species, crystallization, graphitization of source powder, growth rate, and internal stress of the grown crystal.

3.2 High-temperature chemical vapor deposition

Essentially, the HTCVD and PVT methods share the same mechanism, in which the vapor species are the intermediate sources for SiC deposition. The difference is that the initial source materials are SiC powder and gases in the PVT and HTCVD methods, respectively. Hence, the HTCVD method is also known as the gas-source method for SiC growth. One advantage of the HTCVD method over the PVT method is that the Si/C ratio of the vapor species is more easily controlled by adjusting the ratio and flow rate of the source gases. Therefore, the HTCVD method is promising for growing SiC crystals at high growth rates.

In simulations of the HTCVD method, the temperature distribution, fluid flow profile, and chemical reactions have been considered. However, the chemical reactions in HTCVD are more important and complicated than those in the PVT, because there are other elements in addition to Si and C in the equilibria. The system of interest is typically ternary (i.e., Si–C–H) or quaternary (e.g., S–C–H–Cl) systems; hence, the chemical reactions are complicated and

commonly calculated separate from the finite analysis with the assumption that the system is in quasi-equilibrium [61]. Common Si–C–H systems are $\text{SiH}_4\text{--C}_3\text{H}_8\text{--H}_2$ [62–65] and TMS--H_2 [29–32, 61].

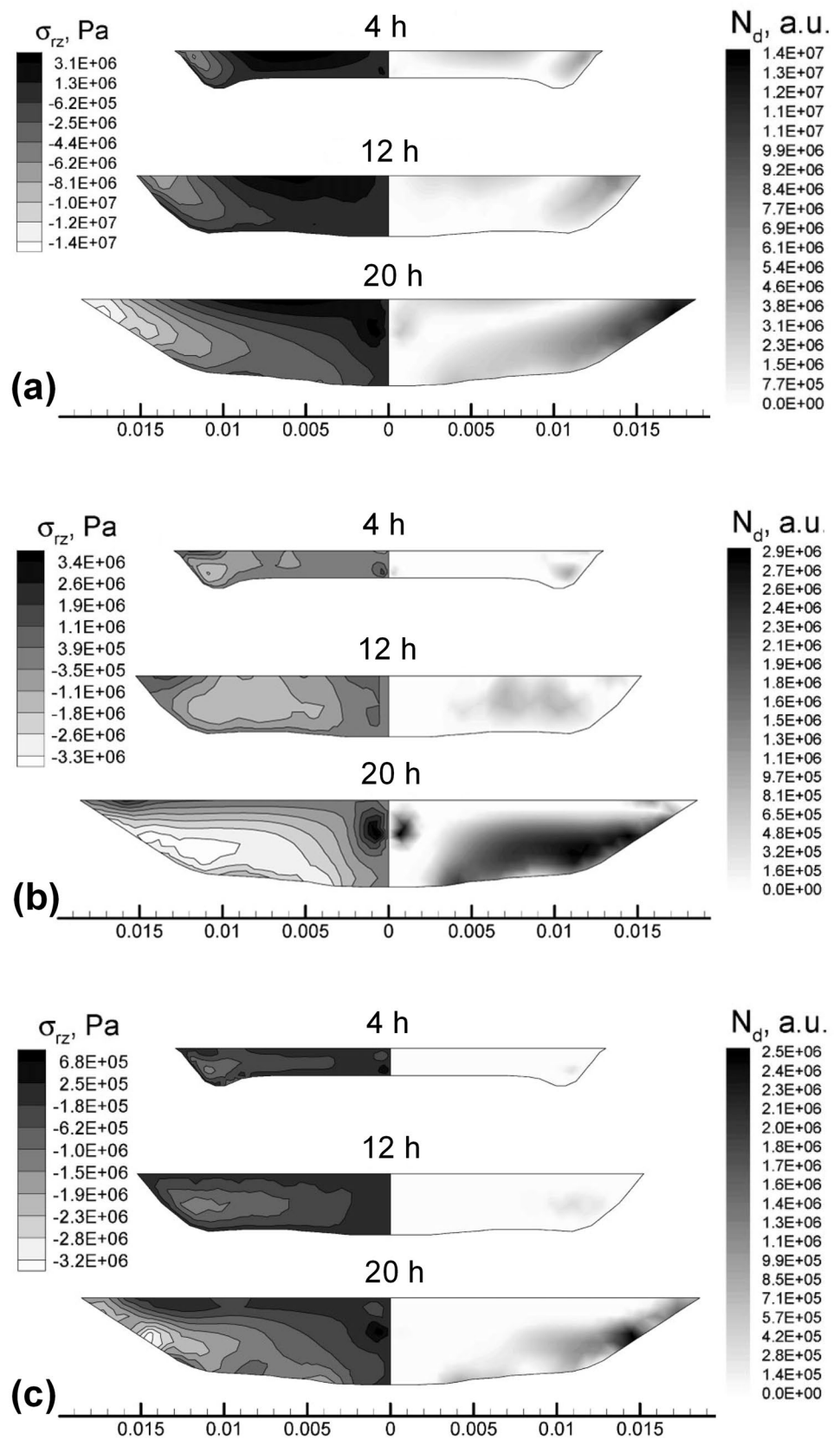
Danielsson et al. and Kito et al. considered a very large number of possible reactions (over 100) in the $\text{SiH}_4\text{--C}_3\text{H}_8\text{--H}_2$ system [62, 66]. They attempted to calculate the partial pressure of major species from the non-finite reaction rate of gas-phase reactions, which is written in the form of the Arrhenius equation (Eq. 22), where A is a pre-exponential factor. Figure 8 shows a comparison of the partial pressures of the main species calculated by different researchers. The major vapor species were identified to be SiC_2 , Si_2C , Si, and C_2H_2 , which are relevant to the thermodynamic equilibrium calculation results obtained by Stinespring et al. [37]:

$$K = AT^n \exp(-E_n/RT) \quad (22)$$

Kojima et al. proposed two possible equilibrium systems to determine the existence of intermediate clusters [67]. In the equilibrium system without clusters, the main vapor species (including Si, SiH, SiH_2 , and C_2H_2) developed at a relatively low temperature of approximately 1300 °C, as shown in Fig. 9a. In contrast, in the cluster-containing equilibrium system, SiC(s) and Si(l) clusters were present before sublimating to vapor species (Si, SiC_2 , Si_2C , and C_2H_2) at temperatures over 2000 °C, as shown in Fig. 9b. The cluster-containing equilibrium system was confirmed by in situ observations inside the reactor at high temperatures. Figure 9c, d show the interior of the reactor before and during gas flow, respectively. An opaque cluster of liquid and solid species in the form of mist was observed when the source gas flowed into the reactor. Furthermore, the growth rate derived from the cluster-containing model agreed well with the experimental growth rate.

Jeong et al. investigated the feasibility of the TMS– H_2 system for $\alpha\text{-SiC}$ single-crystal growth [29–31]. They found that the working pressure and Si/H ratio significantly affected the composition of species in the TMS– H_2 system. As shown in Fig. 10a, at a low working pressure and high Si/H ratio ($P = 1 \times 10^{-3}$ atm, $\text{Si/H} = 7.14 \times 10^{-2}$), a C-rich three-phase equilibrium (C(s)–SiC(s)–vapors) occurred at temperatures below 2500 °C. Above this temperature, Si was saturated and did not contribute to crystal growth. However, at near atmospheric pressure and a low Si/H ratio ($P = 1$ atm, $\text{Si/H} = 4.97 \times 10^{-4}$), a Si-rich three-phase equilibrium (SiC(s)–Si(l)–vapors) existed from 1800 to 2100 °C, which supported crystal growth, as shown in Fig. 10b [31]. The effects of the Si/H ratio and working pressure on SiC crystal growth are shown in Fig. 10c, d, respectively [31]. A pure SiC region formed only at relatively high pressures and low Si/H ratios. At relatively low

Fig. 7 Evolution of the stress component (σ_{rz}) and dimensionless dislocation density (N_d) in the growing crystal for **a** fixed axial and radial displacement, **b** free radial displacement, and **c** free axial and radial displacement [57]



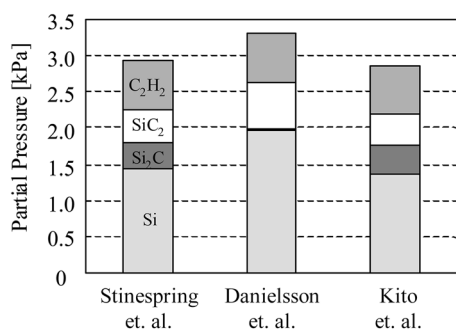


Fig. 8 Partial pressures of the main species calculated by the equilibrium reaction model (Stinespring et al.) and the gas-phase reactions models (Danielsson et al. and Kito et al.) at 2500 °C [37, 62, 66]

temperatures, C was deposited on or incorporated in the SiC crystal, as observed by Kim et al. and Yoon et al. [32, 33]. However, the graphite parts in the reactor were etched under highly Si-rich conditions at relatively high temperatures [32, 62]. Furthermore, by adjusting the Si/H ratio and working pressure ($\text{Si}/\text{H} = 1 \times 10^{-3}$, $P = 0.1$ atm), the growth temperature was stable in the range 2000–2300 °C. Thus, low Si/H and C/Si ratios are crucial for SiC crystal growth in the Si–C–H system.

The Si–C–H–Cl system was considered for the growth of SiC crystals from gas sources [68–71]. Fanton et al. calculated the thermodynamic equilibria of species in the $\text{SiCl}_4\text{--CH}_4\text{--H}_2$ system at 2025 °C for various CH_4 flow rates [68]. When the C/Si ratio was larger than 1, a C-rich condition developed, and polycrystalline growth occurred, as shown in Fig. 11a. The experimental results showed that the boundary between single-crystalline and polycrystalline growth was very abrupt. As shown in Fig. 11b, c, single-crystal step-flow growth was observed at a C/Si ratio of 0.78, which rapidly changed to polycrystalline growth at a C/Si ratio of 0.96. Kito et al. also investigated the $\text{SiCl}_4\text{--C}_3\text{H}_8\text{--H}_2$ system and found that the main species (including Si, Si_2C , and SiC_2) have smaller partial pressures than those in the $\text{SiH}_4\text{--C}_3\text{H}_8\text{--H}_2$ system. Hence, the growth rate in SiCl_4 -based systems is lower than that in SiH_4 -based systems.

In addition, Kang et al. evaluated the thermodynamic equilibria of the MTS--H_2 system using the FactPS database [61, 72]. The thermodynamic equilibrium of the species shown in Fig. 12a indicates that the pure SiC phase is stable at 1900–2200 °C with a H/Si ratio higher than 1000. Compared to the TMS-based system, the MTS-based system has a wider range of suitable process conditions, as shown in Fig. 12b, c. The MTS system is more likely to work at a lower H/Si ratio owing to the stoichiometry of the MTS molecule, which has one C atom for each Si atom. Hence, MTS is a feasible precursor for SiC growth using HTCVD.

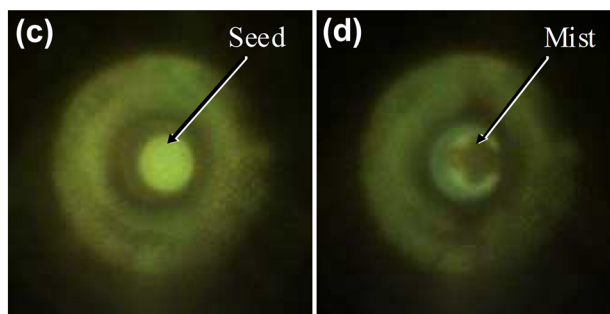
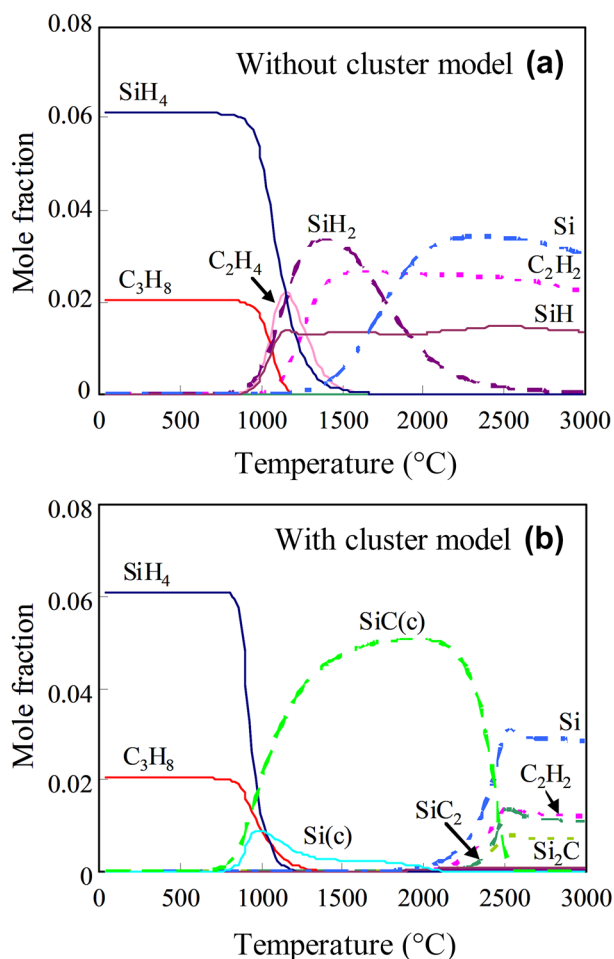


Fig. 9 Calculated mole fraction vs. growth temperature for models **a** without and **b** with clusters. Captured images of the reactor interior **c** before and **d** under source gas flow [67]

The temperature distribution near the seed surface plays an important role in SiC crystal growth by HTCVD. Tokuda et al. focused on the heat flux at the seed crystal during growth [14, 65]. At the crystal surface, the influx and efflux are in equilibrium, as expressed by Eq. (23). Q_{efflux} is the heat transferred to the back side of the crystal, Q_{gas} is the conductive heat from the gas, Q_{rad} is the radiative heat from the influx, and Q_{latent} is the latent heat. If the temperature gradient was not sufficiently large or even negative,

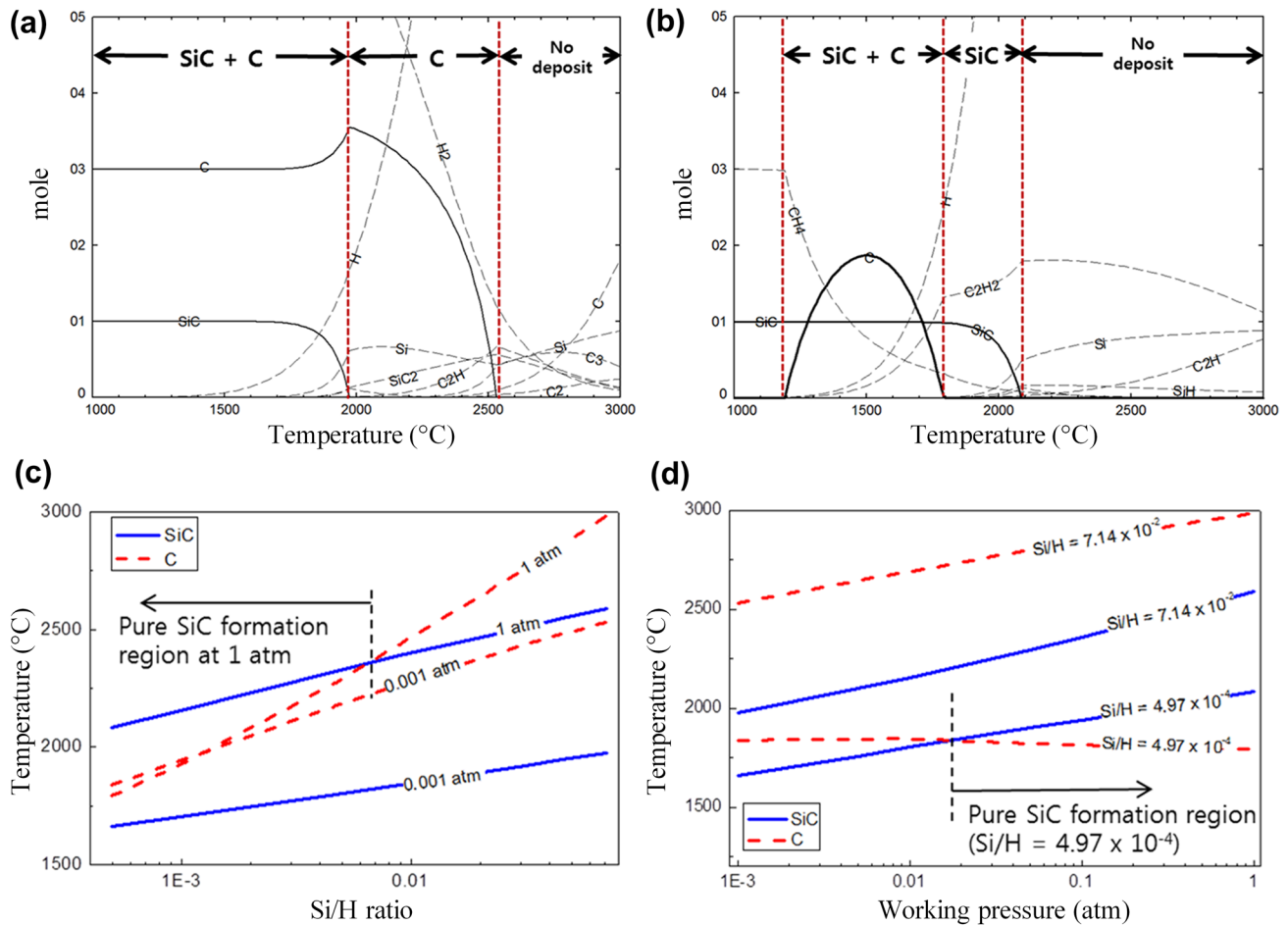


Fig. 10 Equilibrium compositions of vapors and solids in the Si-C-H system as a function of temperature ($T=1000\text{--}2000\text{ K}$) for **a** $\text{Si}/\text{H}=7.14\times 10^{-2}$ and $P=0.001\text{ atm}$ and **b** $\text{Si}/\text{H}=4.97\times 10^{-4}$ and

$P=1\text{ atm}$. Evolution of the maximum temperature of solid SiC and solid C as a function of the **c** Si/H ratio and **d** working pressure calculated by thermodynamic modeling [31]

polycrystalline inclusions or even dendrite crystals were obtained, as shown in Fig. 13. Furthermore, the growth rate was dependent on the partial pressures of the precursors, and a crystal was grown with a growth rate of as fast as 2.4 mm/h (Fig. 13c) using the SiH_4 -based system:

$$Q_{\text{efflux}} = Q_{\text{influx}} = Q_{\text{gas}} + Q_{\text{rad}} + Q_{\text{latent}} \quad (23)$$

Okamoto et al. investigated the relationship of the shape and temperature gradient of a crystal with the internal stress [73]. The convex-shaped crystal, which is common for HTCVD, had higher thermal stress than that of the flat crystal. By decreasing the temperature gradient in the crystal, the stress in the crystal decreased markedly, as shown in Fig. 14.

Understanding and optimizing the vapor species composition are critical for HTCVD. The source gas system and

flow rate must be carefully selected, and the temperature distribution, reactor cell, and seed surface significantly affect the crystal quality. The advantages of the HTCVD method are its high growth rate and feasibility for continuous feeding growth.

3.3 Top-seeded solution growth

In the TSSG method, the important behaviors are C solubility and C transport in the melt. Hence, the heat-transfer coupled fluid dynamics calculation is central to the simulation of the TSSG method. The Navier–Stokes equation (Eq. 10) is the governing equation describing the melt flow in the TSSG method. The term F_{ext} , the total volume force acting on the melt, is the sum of the buoyancy, centrifugal, and Lorentz (electromagnetic) forces. In addition, the Marangoni force at the free surface of the melt must be considered [74–76]. The buoyancy force is present in almost every crystal growth system owing to the temperature gradient in the

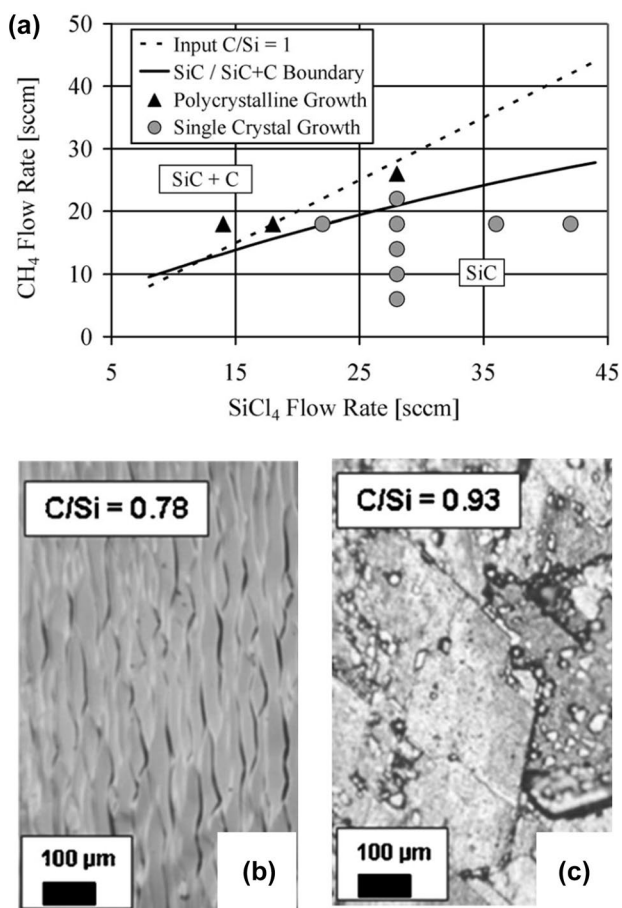


Fig. 11 a Thermodynamic equilibrium of solid and vapor species at 2025 °C and 400 Torr with respect to the CH₄ flow rate. The flow rates of SiCl₄, H₂, and Ar were constant at 29, 500, and 1500 sccm, respectively. **b, c** Surface morphology of crystals grown on 4° off-axis 4H substrates with the C/Si ratios of 0.78 and 0.93, respectively [68]

solution, and the centrifugal force is related to the rotation of the seed crystal and the crucible. The Lorentz force is a side effect of induction heating; it is affected by the induction coil frequency and the current density of the melt [77]. The buoyancy and Lorentz forces are the dominant forces in the melt and define the global melt flow [78, 79], whereas the Marangoni force causes instability in the melt flow, particularly near the crystal edge [76, 80].

The melt flow plays an important role in the C concentration distribution and the crystal growth rate. Lefebure et al. calculated the C concentration and supersaturation distributions in the melt under certain boundary conditions. The C concentration at the crucible–melt and crystal–melt interfaces was set to the C solubility at a certain temperature, assuming that quasi-equilibrium occurs at these interfaces [81]. The C supersaturation (*S*), defined as the difference or ratio between the local C concentration and solubility, indicates the local crystallization (of

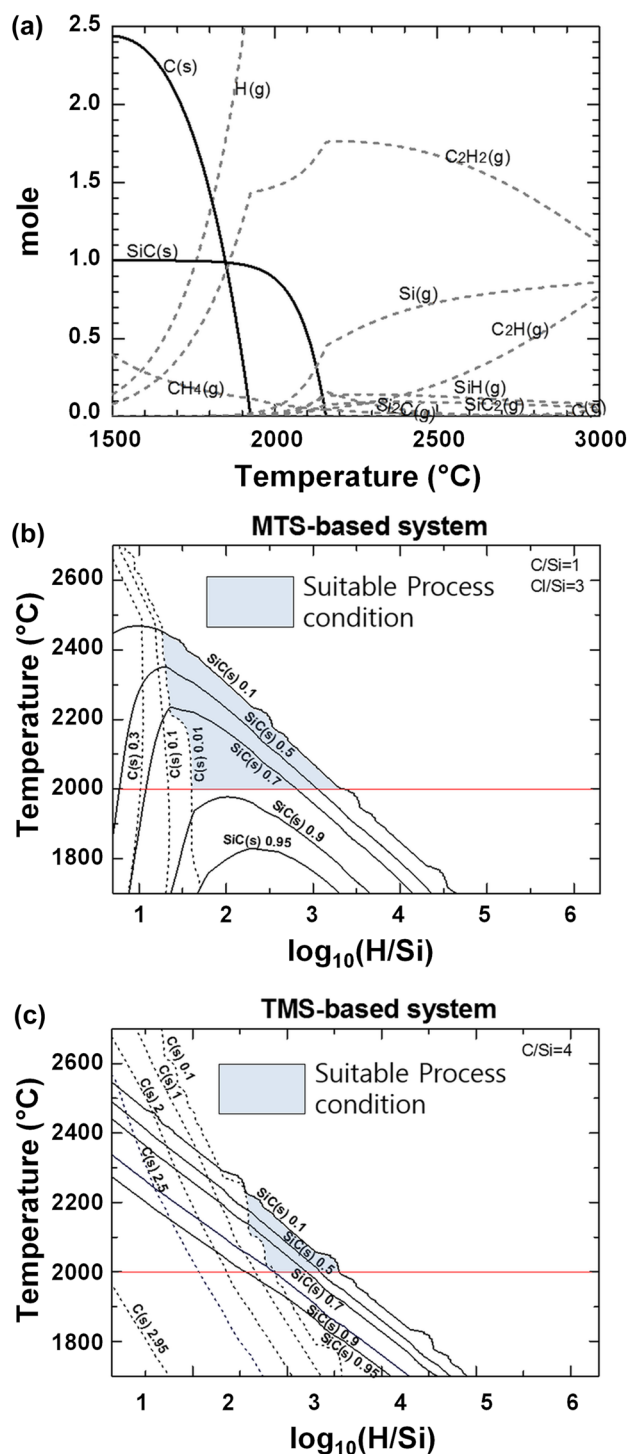


Fig. 12 a Thermal equilibrium of vapors and solids in the Si–C–H–Cl system with respect to temperature (*T*) under a working pressure of 1 atm; the ratios of C/Si, Cl/Si, and H/Si were fixed at 4, 1, and 1000, respectively. **b** Equilibrium amount of solid SiC with respect to temperature and H/Si ratio under a working pressure of 550 Torr in the Si–C–H–Cl system using MTS [61]

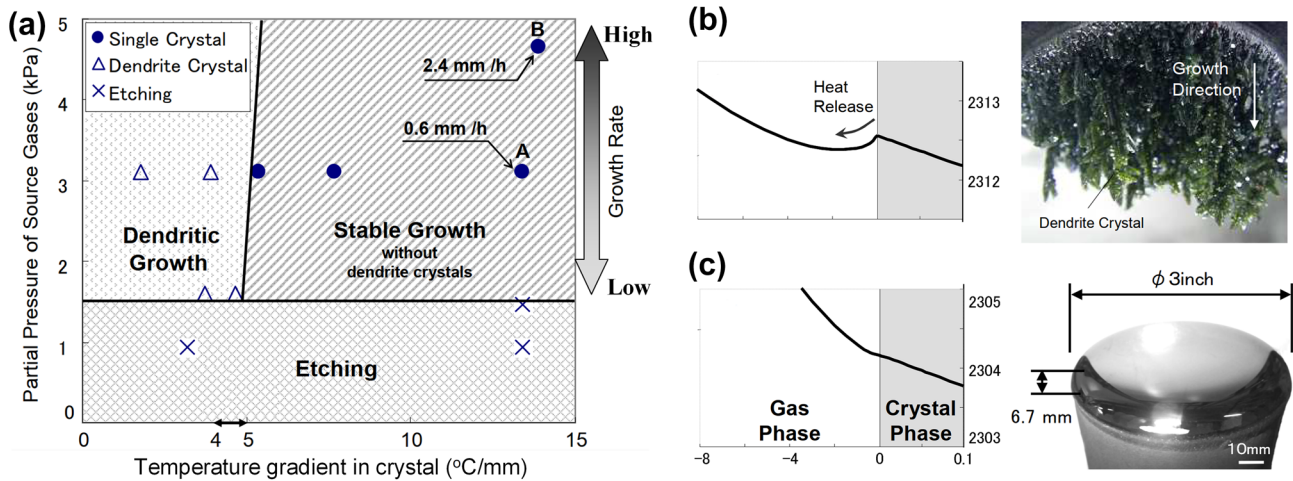


Fig. 13 a Domains of crystal (stable) growth and dendritic growth with respect to the temperature gradient in the crystal and the pressure of the source gases. Calculated temperature distribution in the

crystal and nearby gas: heat flux from **b** crystal to gas (dendritic growth) and **c** gas to crystal (crystalline growth) [14]

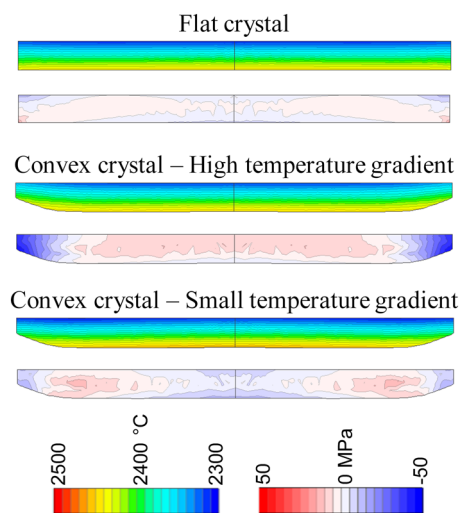


Fig. 14 Temperature and stress distributions in crystals with different shapes and temperature gradients [73]

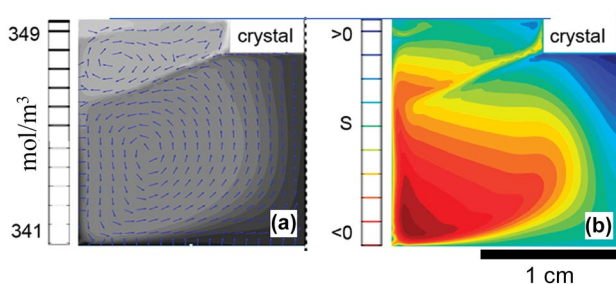


Fig. 15 a C concentration and **b** C supersaturation in the melt at 1900 °C [81]

SiC) or dissolution (of C) regions in the melt, as shown in Fig. 15b. In this setup, the crucible had a low C supersaturation, indicating C dissolved from the crucible into the melt. However, the region below the crystal had a high C supersaturation, resulting in crystal growth. Moreover, a high C supersaturation was observed at the crystal edge, suggesting that parasitic polycrystalline growth could occur at the edge.

The growth rate (G) was estimated by the total C flux (F) perpendicular to the crystal, which has area S , as expressed in Eq. 13. Lefebure et al. assumed that all C atoms that reach the surface contribute to crystal growth without any kinetic limitation. In addition, Ha et al. included the probability (P_s) of C atoms sticking to the crystal surface (Eq. 24–25), which is related to the adsorption energy of C atoms on the crystal surface:

$$G = \frac{M_{\text{SiC}}}{\rho \pi r^2} \iint_S P_s F(r) dS \quad (24)$$

$$P_s = A \cdot \exp(-E_a/RT) \quad (25)$$

Several efforts have been made to increase the growth rate by enhancing the C solubility in the binary solvent [38, 82, 83]. As shown in Fig. 16a, the calculated C solubility in Si–X solvents increases as the ratio of X metal increases, where X is Cr, Ti, Fe, Co, Ni, Zr, Mo, W, and Y [38]. Among them, Si–Fe, Si–Co, and Si–Ni solvents have the lowest C solubilities. In contrast, stable solid phases, such as ZrC, MoSi₂, and WSi₂, were formed at high temperatures in the Zr–Si–C, Mo–Si–C, and W–Si–C systems, respectively. Moreover, concentrations of Cr, Ti, and Y impurities in the

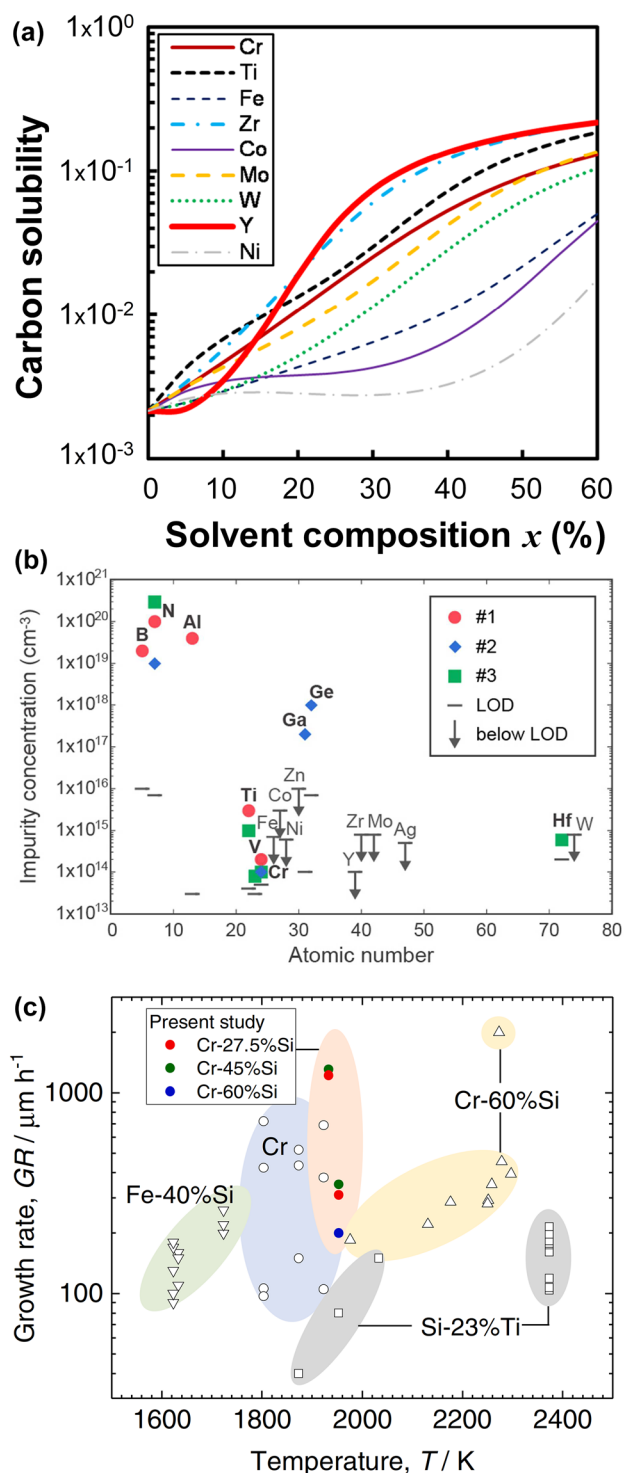


Fig. 16 **a** Calculated C solubility for various solvents ($\text{Si}-x\% \text{X}$; $\text{X}=\text{Cr}, \text{Ti}, \text{Fe}, \text{Zr}, \text{Co}, \text{Mo}, \text{W}, \text{Y}, \text{Ni}$) at 1800°C . **b** Impurity concentration in the SiC crystal for several metals [38]. **c** Growth rate survey for different solvents and temperatures [83]

grown SiC crystals were negligible, as shown in Fig. 16b [38]. Hence, the metals of Ti, Cr, and Y are feasible for Si-X solvents with high C solubility.

A high C concentration and C dissolution rate in the melt are crucial for improving the SiC crystal growth rate. Lee et al. found that the C dissolution process involves the infiltration of the Si melt into the graphite crucible, the diffusion of C into the melt, and the formation of a SiC interlayer near the crucible wall [84]. Hence, a high-porosity graphite crucible will improve the infiltration of the Si melt and C dissolution. Choi et al. used a stepped-wall crucible, which has a higher crucible–melt interfacial area that enhances C dissolution [85].

The temperature gradient in the melt is an important factor affecting the growth rate and crystal quality. Numerous efforts have been made to optimize the thermal distribution in the melt by adjusting the apparatus design at different scales, such as hot zones [86–88], crucibles [74, 89, 90], shafts [91], and the melt meniscus [92]. Ha et al. investigated the effects of hot-zone structures on the temperature gradient in the melt and the quality of the grown crystals [87]. There were significant differences in the temperature distribution between the compact (SI) and extended (LI) hot zones, as illustrated in Fig. 17a. As shown in Fig. 17b, c, temperature and C supersaturation boundary layers were present at the crystal–melt interface. The temperature and C supersaturation gradient were steeper for the SI case, suggesting that a compact hot zone increases the temperature gradient, C saturation, and growth rate, as shown in Fig. 17d. However, a very high temperature gradient causes the formation of rough polycrystalline SiC. Hence, there is a trade-off between the growth rate and crystal quality for SiC crystals growth via the TSSG method.

Kim et al. and Liu et al. suggested complex crucible designs, as illustrated in Fig. 18 [89, 90]. These designs can be tuned to achieve the appropriate temperature gradient and C concentration in their specific crystal growth equipment.

Fujii et al. controlled the temperature gradient by changing the conductivity of the shaft [91]. As shown in Fig. 19a, the temperature gradient in the melt was higher with a solid seed shaft. Moreover, the lateral temperature gradient increased, resulting in parasitic crystal growth at the edge. The hollow shaft provided a more uniform temperature gradient and a smooth crystal surface.

Kusunoki et al. investigated the temperature gradient with different meniscus heights, as illustrated in Fig. 19b [92]. Both the axial and radial temperature gradients increased markedly with increasing meniscus height. Hence, a high meniscus can enhance the crystal growth rate, but it also increases the probability of parasitic crystal growth at the edge of the crystal or the formation of an unfavorable concave crystal shape [93].

Because the growth rate of SiC crystals in the TSSG method is dependent on C transport from the crucible to the seed crystal, several efforts have been made to enhance the transport efficiency. Umezaki et al. confirmed that

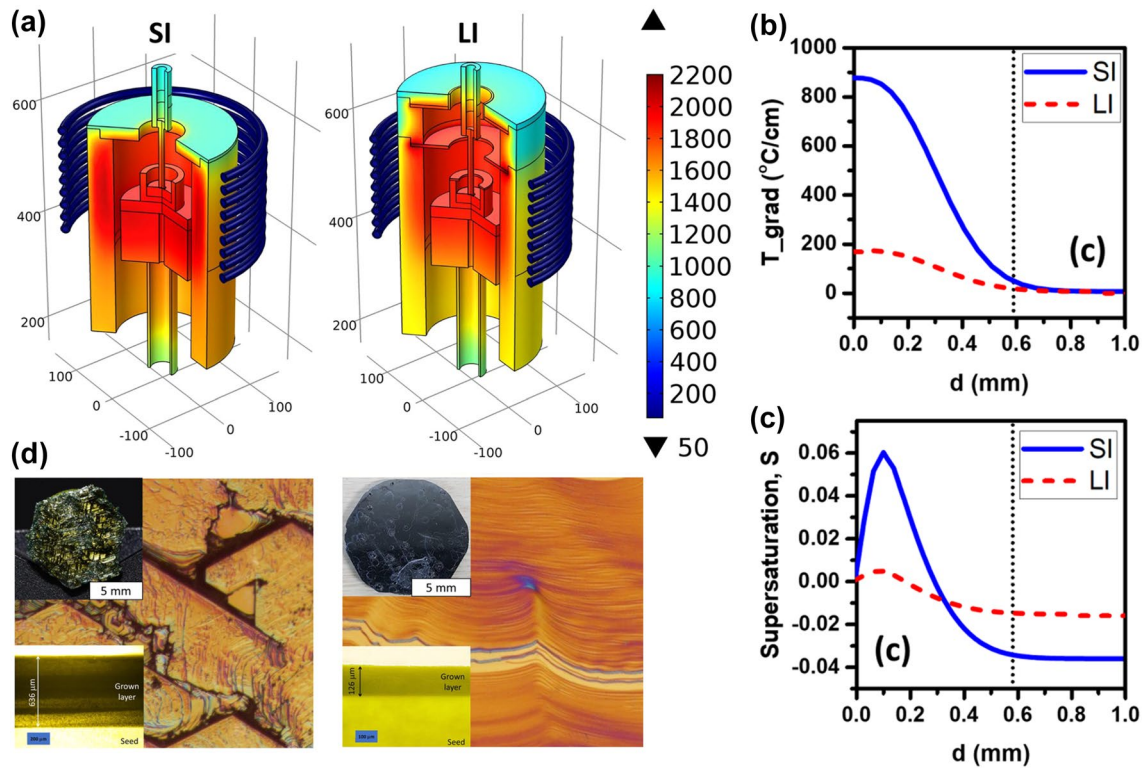
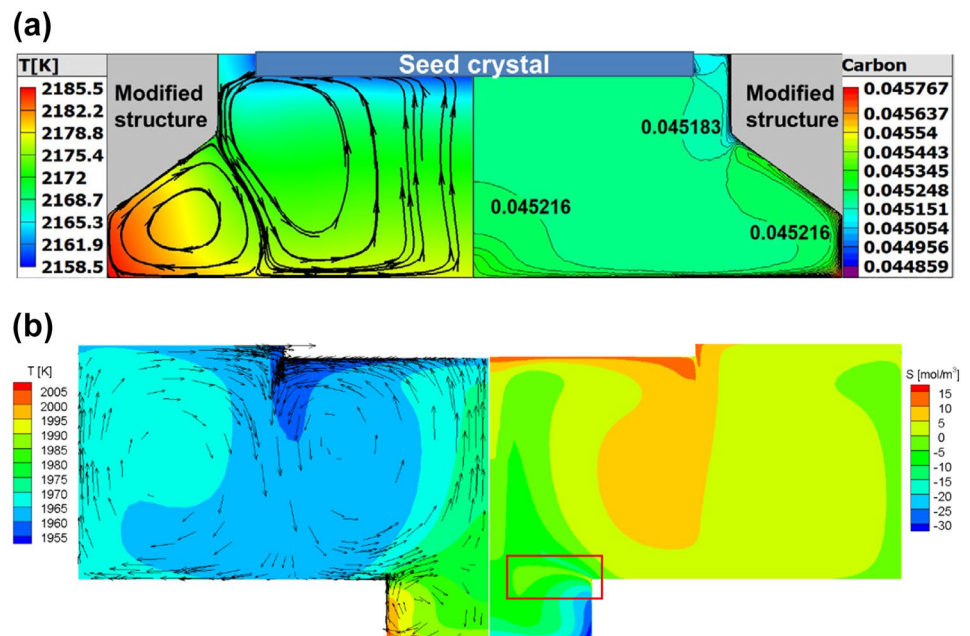


Fig. 17 **a** Temperature distribution in a short (SI) and an extended (LI) hot zone. **b** Temperature gradient and **c** supersaturation near the crystal–melt interface. **d** Photographs, surface morphology, and thickness of grown crystals [86]

Fig. 18 Temperature and C distributions in the melt with different crucible structures conducted by **a** Kim et al. [89] and **b** Liu et al. [90]



high-speed rotation of the seed crystal reduces the boundary layer at the crystal surface, resulting in a steeper C concentration gradient at the surface. Hence, the growth rate is linearly proportional to the C concentration gradient [94].

Kusunoki et al. and Kurashige et al. assessed the accelerated crucible rotation technique (ACRT) for TSSG of SiC crystals [95, 96]. In the ACRT, the rotation rate of the crucible is periodically accelerated, decelerated, and inverted, as

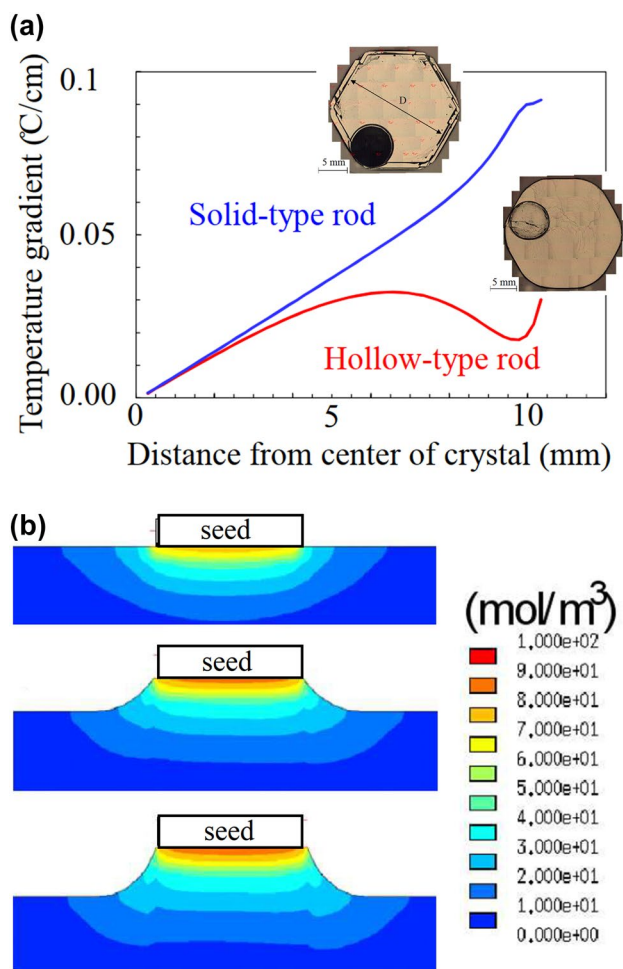


Fig. 19 a Temperature gradient in the melt and resultant crystals with solid and hollow seed shafts [91]. b Temperature gradient with different meniscus heights [92]

shown in Fig. 20a. In the conventional ACRT, the melt flow direction under the seed crystal changes from downward to upward during the acceleration and deceleration periods, respectively, as shown in Fig. 20b, c. Changing the flow direction enhances C transport from the bottom of the crucible to the seed crystal.

Another approach to improve C transport is to structurally alter the crucible. Kurashige et al. inserted a thin plate at the bottom of a crucible, as shown in Fig. 20d, e. Because the velocities of the upper and lower halves of the melt were different, a vortex flowed counterclockwise and clockwise near the crucible wall during the acceleration and deceleration periods, respectively. The vortex increased C transport from the crucible wall to the seed crystal, which remarkably improved the growth rate and crystal quality, as shown in Fig. 20f, g. Polycrystalline SiC was obtained using the non-ACRT process, whereas smooth crystals with growth rates of 60 and 110 $\mu\text{m/h}$ were achieved using the ACRT process without and with an additional plate, respectively.

Kusunoki et al. implanted a graphite ring inside the crucible, separating the melt into the upper and lower halves [92]. Under an appropriate temperature gradient, they improved the C concentration in the upper half of the melt, resulting in a 50% enhancement in the growth rate.

Ha et al. deployed a flow modifier with a hollow cone shape inside the crucible to redirect the melt flow [76]. The melt flow is typically strong near the crucible wall and forms vortices, as shown in Fig. 21a–a1. The flow modifier acted as an obstacle, confining the flow at the crucible wall (Fig. 21b–b1), or as a guide, directing the flow from the crucible wall to the seed (Fig. 21c–c1). As a result, the downward-placed flow modifier enhanced C transport from the crucible wall to near the seed (C accumulation region), creating a virtual C source beneath the growth front, as

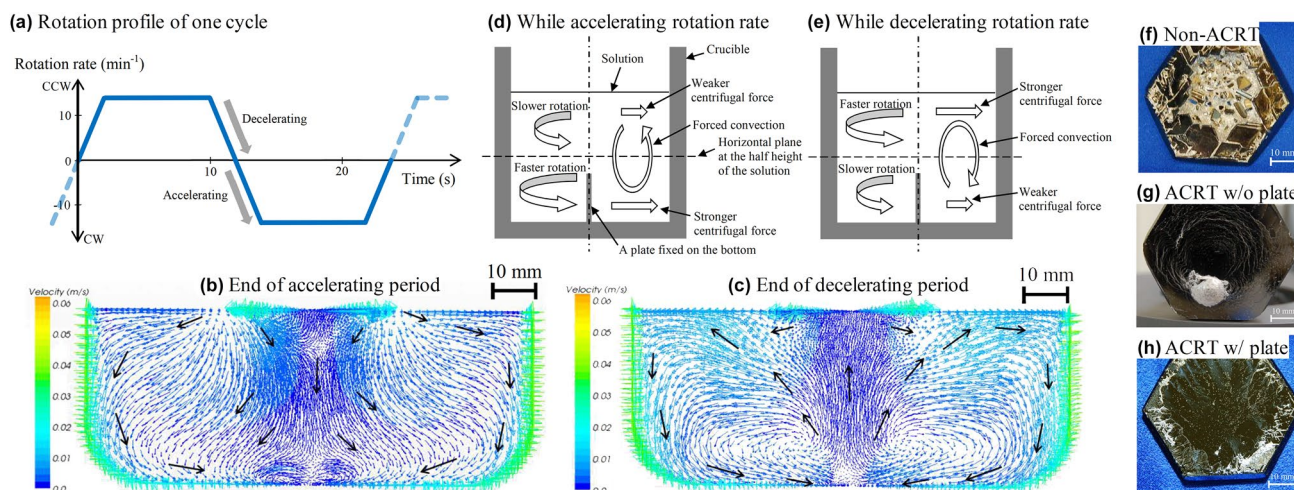


Fig. 20 a Rotation rate of one ACRT cycle. b–e Simulated flows during acceleration and deceleration. Photographs of samples grown under different conditions: f non-ACRT, g ACRT without a divider plate, and h ACRT with a divider plate [96]

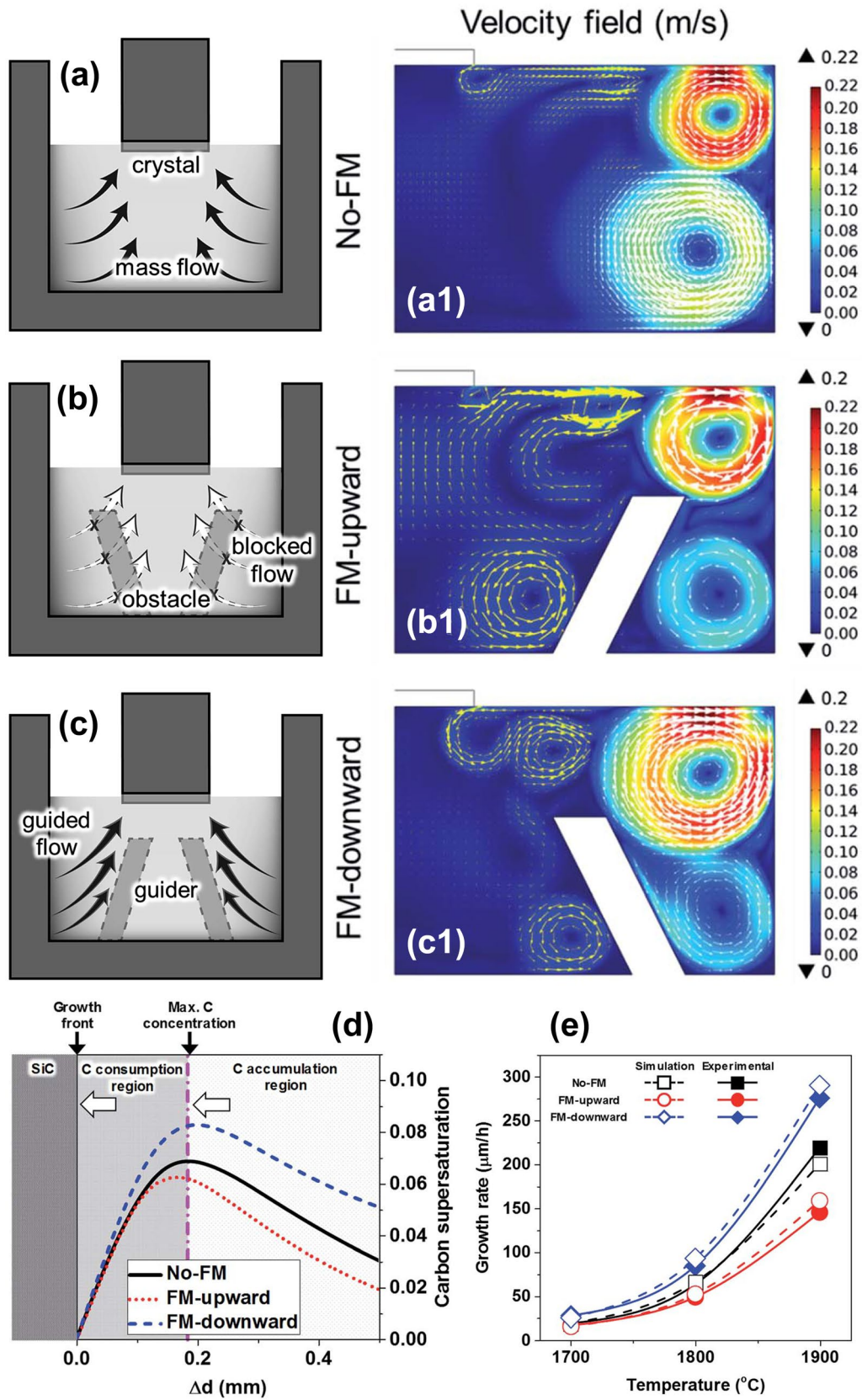


Fig. 21 Schematic for **a** conventional crucible setup and those with a fluid modifier (FM) placed **b** upward and **c** downward. **a1–c1** Velocity fields for the respective cases. **d** C supersaturation distribution in

the melt near the crystal surface. **e** Comparison between simulated and measured growth rates [76]

shown in Fig. 21d. The C from the virtual source diffused to the growth front and contributed to crystal growth, defining the C consumption region. The calculated growth rate from this model agreed well with the experimental growth rate, as shown in Fig. 21e, indicating that the downward-placed flow modifier remarkably enhanced the crystal growth rate. Hence, by optimizing the melt flow, the crystal growth rate was significantly improved.

Another challenge for SiC growth via the TSSG method is growth rate uniformity. Non-uniform growth rate leads to

a curved crystal surface (convex, concave, or wavy) or undesirable parasitic crystals on the edge of the boule. Marangoni convection is considered to be the main reason for the non-uniform growth rate [76, 80]. Hence, many efforts have been made to minimize this effect.

Marangoni convection commonly has a centripetal direction, as shown in Fig. 22a [76]. Hence, a sufficiently large centrifugal convection would theoretically suppress Marangoni convection. However, in popular growth systems, the centrifugal force (Fig. 22b) is substantially smaller than

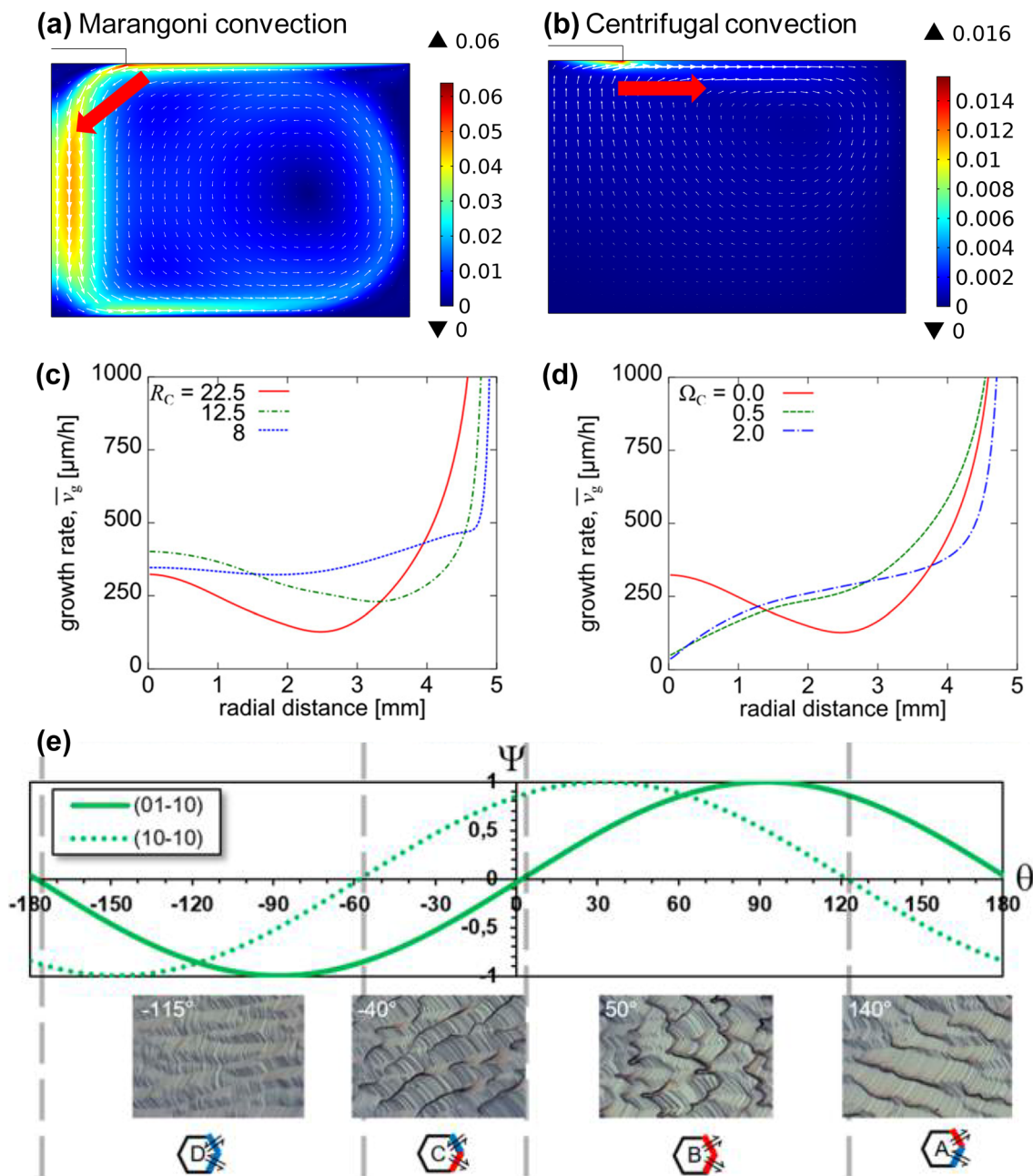


Fig. 22 Velocity field from **a** Marangoni and **b** centrifugal convections [76]. Crystal growth rate profile (axial direction) for different **c** stationary crucible sizes and **d** crucible rotation rates [97]. **e** Step growth direction vs. flow direction [98]

the Marangoni force. The seed rotation speed required for centrifugal convection to suppress Marangoni convection is considered impractical.

Horiuchi et al. noted that a smaller crucible diameter reduces Marangoni convection, resulting in more uniform crystal growth (Fig. 22c) [97]. However, increasing the crucible rotation rate decreases the crystal growth rate at the center of the crystal, further deteriorating the uniformity, as plotted in Fig. 22d. Ariyawong et al. investigated the relationship between the propagation of a crystal micro-step and the melt flow direction [98]. The melt flow direction relative to the crystal as a function of the seed rotation speed is

plotted in Fig. 22e. The flow parallels to step propagation causes a rough crystal surface, whereas the anti-parallel flow supports a smooth crystal surface [93, 99, 100].

Wang et al. and Ha et al. numerically assessed the potential of advanced magnetic fields to improve crystal growth rate uniformity [101, 102]. Depending on the relative position of the induction coil and the crucible, the magnetic field passing through the melt can have a vertical (Fig. 23a, b) or cusp (Fig. 23c, d) orientation. Moreover, if additional Helmholtz coils are used, the desired magnetic field configuration can be achieved through the electric current direction in the Helmholtz coils, as illustrated in Fig. 23 [102]. The

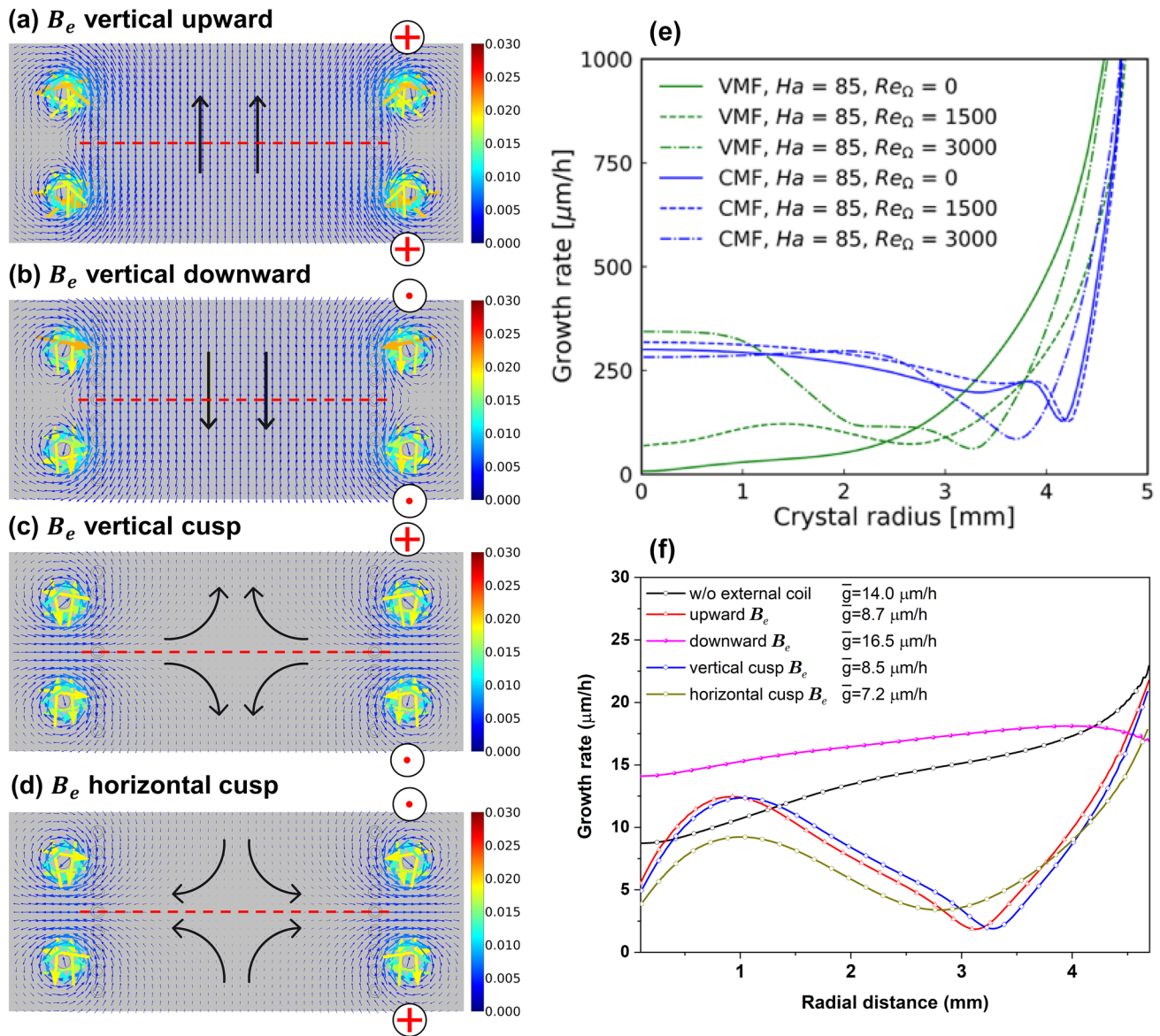


Fig. 23 Different static magnetic field configurations: **a** vertical upward, **b** vertical downward, **c** vertical cusp, and **d** horizontal cusp [102]. Crystal growth rate along the radial direction for different mag-

netic field configurations at **e** 2100 °C [101] and **f** 1800 °C [102]. B_e external magnetic field, VMF vertical magnetic field, CMF cusp magnetic field, \bar{g} mean growth rate

Lorentz forces generated by the cusp-oriented (horizontal) magnetic field suppress the Marangoni force at the crystal edge, enhancing the melt flow stability at the growth front. Hence, the growth rate uniformity is significantly improved for the cusp-oriented (horizontal) magnetic field configuration. In contrast, a vertically oriented magnetic field reduces the uniformity of the growth rate.

In the TSSG of SiC, the residual Si droplets on the crystal surface cause stress-related problems. Owing to the different thermal expansion behaviors of Si and SiC, a stress field is generated during cooling after crystal growth. The stress is substantial at the edge of the droplet (Fig. 24b), resulting in defects, such as micro-pipes and cracks. Ha et al. suggested a post-heat treatment procedure, that is, slow cooling for droplet evaporation, to remove droplets on the crystal surface [103]. The X-ray diffraction (XRD) patterns in Fig. 24d indicate that the internal stress in the droplet-free crystal

(sample B) was smaller than that in the droplet-containing crystal (sample A). Internal stress remained in sample B because of the different thermal expansion behaviors of the SiC crystal and the graphite shaft.

Briefly, the C solubility is the most important factor determining the crystal growth rate in the TSSG method, and it has been improved by several approaches, such as composition and crucible design. The C transport in the melt has been optimized to improve the growth rate and crystal uniformity. Although the quality of crystals grown by the TSSG method is typically high, a post-heat treatment should be conducted to preserve the quality.

4 Recent advances in machine learning for SiC crystal growth

Currently, machine learning (ML) and artificial intelligence (AI) algorithms are becoming mature, opening a new route for crystal growth process design and optimization, as well as real-time adjustments. In general, computational fluid dynamics (CFD)-based simulations of the TSSG of SiC crystals require considerable time and computational resources. Hence, CFD-based simulations lack the flexibility required for optimization. In contrast, an ML model, which learns from pre-calculated sets of CFD-based simulations, responds quickly to process parameter changes. Ujihara et al. actively developed an ML procedure for SiC crystal growth by TSSG. The very first report was published in 2018, which used a modern convolutional neural network (CNN) to learn a prepared set of data (800 CFD-based samples) [104]. A general schematic of the CNN model for SiC crystal growth is shown in Fig. 25a. The input was vectorized parameters, such as temperature, rotation speed, and crystal diameter. The number of hidden layers and hidden nodes were 4 and 128, respectively. The output parameters were the temperature distribution, concentration profile, and velocity components. As shown in Fig. 25b, c, the predicted results were similar to the CFD-based result, with a correlation coefficient (which measures the difference between the result predicted from ML and that predicted by CFD) of more than 0.9 (where 1 indicates perfect matching). Moreover, the prediction time was rapid (sub-second), emphasizing the potential for real-time prediction and optimization.

Wang et al. improved the ML process using a reinforcement learning model, in which the ML process and CFD calculation feed data to each other in a calculation loop [105]. Hence, both the ML process and CFD calculation were faster with more accurate results. Horiuchi et al. and Takehara et al. further improved the ML process by implementing Gaussian optimization to create a complete Bayesian optimization procedure for SiC crystal growth, as shown

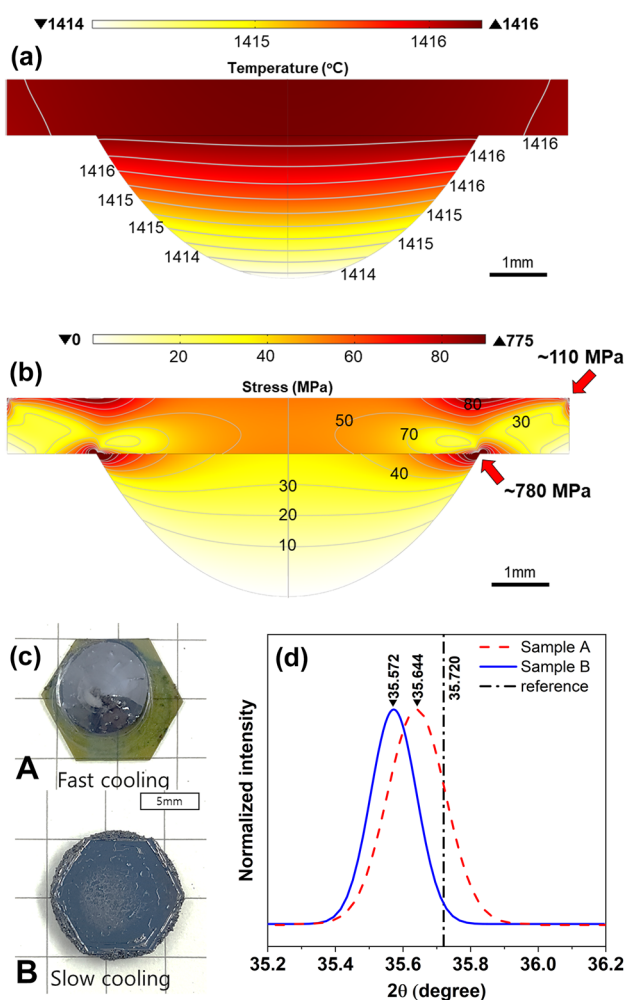


Fig. 24 **a** Temperature distribution in a liquid droplet during solidification and **b** stress distribution in the droplet at room temperature. **c** Photographs and **d** XRD patterns of crystals cooled at fast and slow rates [103]

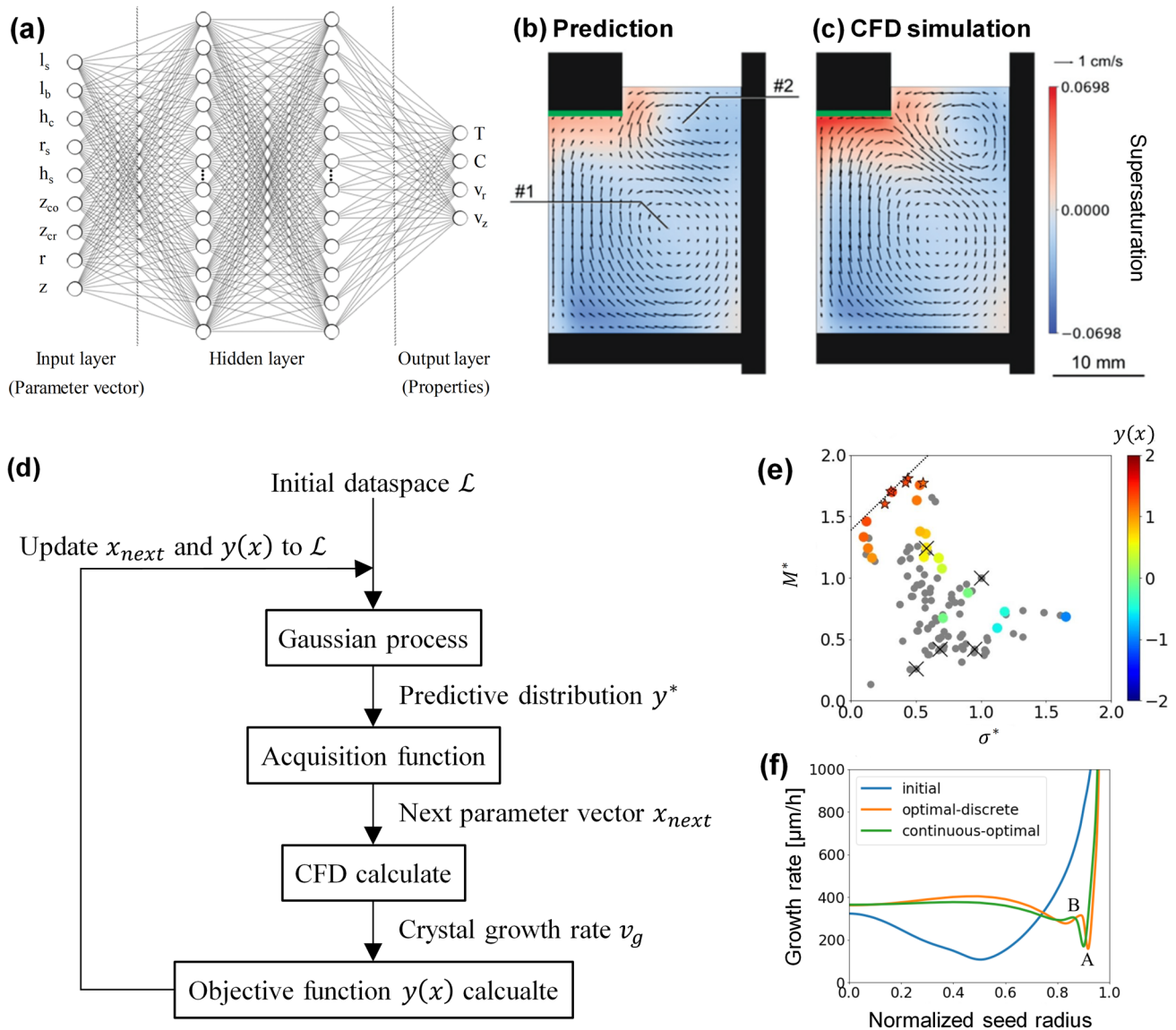


Fig. 25 **a** CNN structure [109] and results from **b** CNN-based prediction and **c** CFD-based calculations [104]. **d** Flow diagram of Bayesian optimization [107]. **e** Distribution of the normalized mean and

deviation of the growth rate profile (M^* and σ^* , respectively). Color bar is the objective function, $y(x)$. **f** Growth rate along the axial direction for initial and optimized parameters [108]

in Fig. 25d [106–108]. In this procedure, an objective function is introduced:

$$y(x) = M^* - \sigma^*, \quad (26)$$

where M^* and σ^* are the normalized mean and deviation of the growth rate profile, respectively. The target is to obtain a high and uniform growth rate, that is, large M^* and small σ^* values. Hence, the goal of the Gaussian process is to find a parameter vector corresponding to the smallest $y(x)$. These data are then passed to the CNN (acquisition function) learning process and CFD calculation. Using this procedure, the ML process was completed in a few tens of iterations when

the objective function $y(x)$ converged, as shown in Fig. 25e, and the growth rate and uniformity theoretically improved, as shown in Fig. 25f.

Using the Bayesian procedure, the optimal process parameters were prepared before crystal growth, including crucible design [109]. However, in practical experiments, the geometry of the crucible also changes because of C dissolution and Si evaporation (Fig. 26a), and the thickness of the crystal also increases. Therefore, real-time prediction, optimization, and tuning are crucial for TSSG. CFD-based calculations of TSSG are a considerable challenge when the model geometry changes because of sensitive and intensive model re-meshing [110]. Dang et al. successfully developed

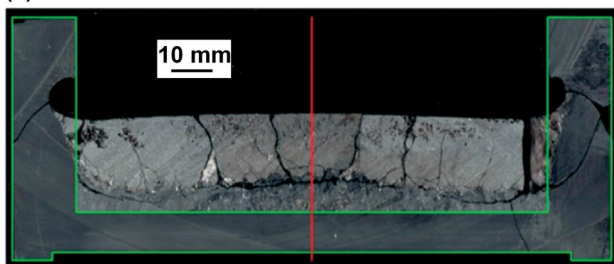
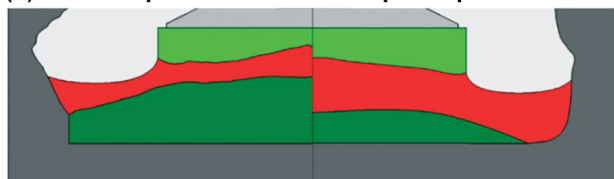
(a) Cross-section of a crucible after 30 hours**(b) Fixed parameters Adaptive optimization**

Fig. 26 **a** Cross-sectional image of a crucible after 30 h of crystal growth. **b** Predicted results for fixed parameters (left side) and adaptive optimization (right side). The light green color is the SiC single crystal, the red color is the melt, and the dark green color is the polycrystal [111]

adaptive optimization and process control for long-term crystal growth [111]. With this technique, the crucible corrosion was reduced, the available growth time increased by 50%, and the crystal yield increased by 30% with a flatter surface, as demonstrated in Fig. 26b.

Machine learning does not replace the numerical simulation for SiC crystal growth. Instead, ML uses the numerical results and accelerates the process design. ML has proven to be effective for quick prediction, supervision, and optimization of SiC crystal growth.

5 Conclusion and future works

Silicon carbide is a next-generation material for high-power and high-efficiency electrical devices. The crystal growth techniques of SiC single crystals have been intensively developed thus far; however, further developments in crystal growth at large scales with high yields and ultra-low defect densities remain ongoing. Simulation techniques have contributed significantly to the investigation of the physicochemical behaviors of SiC crystal growth, including the temperature distribution, chemical species equilibrium, and mass transport. Therefore, process design and optimization based on simulation techniques are now the core technology of SiC crystal growth, particularly for industrial mass production.

As shown in this review, the recent progress in machine learning proves its usefulness as a supplemental technique to the conventional finite-element methods, especially for the

crystal growth of SiC. Besides, hybrid simulation techniques coupling machine learning, FEM, and thermodynamic calculations are currently actively developed by many research groups. We estimate general users could access the hybrid simulation technique provided by some commercialized simulation soon. We believe that the advancement of the simulation technique could drastically reduce the cost and the efforts in the research and development of single crystals and growers requiring intensive investment.

Declarations

Conflict of interest The authors have no relevant financial or non-financial interests to disclose.

References

1. Z.C. Feng, *SiC power materials devices and applications* (Springer, Berlin, 2004). (ISBN: 978-3-662-09877-6)
2. Z.C. Feng, J.H. Zhao (eds.), *Silicon carbide: materials, processing, and devices* (Taylor & Francis, New York, 2004). (ISBN: 978-1-59169-023-8)
3. S.E. Sadow, A. Agarwal (eds.), *Advances in silicon carbide processing and applications* (Artech House, Boston, 2004). (ISBN: 978-1-58053-740-7)
4. M.B.J. Wijesundara, R. Azevedo, *Silicon carbide microsystems for harsh environments* (Springer, New York, 2011). (ISBN: 978-1-4419-7120-3)
5. T. Kimoto, J.A. Cooper, *Fundamentals of silicon carbide technology: growth, characterization, devices and applications* (John Wiley & Sons Singapore Pte Ltd, Singapore, 2014). (ISBN: 978-1-118-31352-7)
6. D.-H. Yoon, I.E. Reimanis, A review on the joining of SiC for high-temperature applications. *J. Korean Ceram. Soc.* **57**, 246–270 (2020). <https://doi.org/10.1007/s43207-020-00021-4>
7. E.G. Acheson, Carborundum: its history, manufacture and uses. *J. Frankl. Inst.* **136**, 194–203 (1893). [https://doi.org/10.1016/0016-0032\(93\)90311-H](https://doi.org/10.1016/0016-0032(93)90311-H)
8. G.R. Fisher, P. Barnes, Towards a unified view of polytypism in silicon carbide. *Philos. Mag.* **B 61**, 217–236 (1990). <https://doi.org/10.1080/13642819008205522>
9. F. Bechstedt, P. Käckell, A. Zywietz, K. Karch, B. Adolph, K. Tenelsen, J. Furthmüller, Polytypism and properties of silicon carbide. *Phys. Status Solidi B* **202**, 35–62 (1997). [https://doi.org/10.1002/1521-3951\(199707\)202:1%3c35::AID-PSSB35%3e3.0.CO;2-8](https://doi.org/10.1002/1521-3951(199707)202:1%3c35::AID-PSSB35%3e3.0.CO;2-8)
10. G.N. Philip, Silicon carbide technology, in *VLSI Handb.*, 2nd edn., ed. by W.-K. Chen (CRC Press, Boca Raton, 2007), p. 5.1-5.34
11. A. Elasser, T.P. Chow, Silicon carbide benefits and advantages for power electronics circuits and systems. *Proc. IEEE* **90**, 969–986 (2002). <https://doi.org/10.1109/JPROC.2002.1021562>
12. Wolfspeed®, HPSI—semi-insulating SiC substrates (2021). <https://www.wolfspeed.com/products/materials/hpsi-semi-insulating-sic-substrates>. Accessed 1 Nov 2021
13. II–VI Incorporated, Silicon carbide (SiC) substrates for power electronics (2021). <https://ii-vi.com/product/sic-substrates/>. Accessed 1 Nov 2021
14. Y. Tokuda, J. Kojima, K. Hara, H. Tsuchida, S. Onda, 4H-SiC bulk growth using high-temperature gas source method. *Mater.*

- Sci. Forum **778–780**, 51–54 (2014). <https://doi.org/10.4028/www.scientific.net/MSF.778-780.51>
15. N. Hoshino, I. Kamata, Y. Tokuda, E. Makino, J. Kojima, H. Tsuchida, Fast 4H-SiC crystal growth by high-temperature gas source method. *Mater. Sci. Forum* **778–780**, 55–58 (2014). <https://doi.org/10.4028/www.scientific.net/MSF.778-780.55>
 16. A.R. Powell, J.J. Sumakeris, Y. Khlebnikov, M.J. Paisley, R.T. Leonard, E. Deyneka, S. Gangwal, J. Ambati, V. Tsevtkov, J. Seaman, A. McClure, C. Horton, O. Kramarenko, V. Sakhalkar, M. O’Loughlin, A.A. Burk, J.Q. Guo, M. Dudley, E. Balkas, Bulk growth of large area SiC crystals. *Mater. Sci. Forum* **858**, 5–10 (2016). <https://doi.org/10.4028/www.scientific.net/MSF.858.5>
 17. T. Mitani, N. Komatsu, T. Takahashi, T. Kato, T. Ujihara, Y. Matsumoto, K. Kurashige, H. Okumura, 4H-SiC growth from Si-Cr-C solution under Al and N Co-doping conditions. *Mater. Sci. Forum* **821–823**, 9–13 (2015). <https://doi.org/10.4028/www.scientific.net/MSF.821-823.9>
 18. K. Kusunoki, N. Okada, K. Kamei, K. Moriguchi, H. Daikoku, M. Kado, H. Sakamoto, T. Bessho, T. Ujihara, Top-seeded solution growth of three-inch-diameter 4H-SiC using convection control technique. *J. Cryst. Growth* **395**, 68–73 (2014). <https://doi.org/10.1016/j.jcrysgro.2014.03.006>
 19. Yu.M. Tairov, V.F. Tsevtkov, Investigation of growth processes of ingots of silicon carbide single crystals. *J. Cryst. Growth* **43**, 209–212 (1978). [https://doi.org/10.1016/0022-0248\(78\)90169-0](https://doi.org/10.1016/0022-0248(78)90169-0)
 20. O. Kordina, C. Hallin, A. Ellison, A.S. Bakin, I.G. Ivanov, A. Henry, R. Yakimova, M. Touminen, A. Vehanen, E. Janzén, High temperature chemical vapor deposition of SiC. *Appl. Phys. Lett.* **69**, 1456 (1996). <https://doi.org/10.1063/1.117613>
 21. D.H. Hofmann, M.H. Müller, Prospects of the use of liquid phase techniques for the growth of bulk silicon carbide crystals. *Mater. Sci. Eng. B* **61–62**, 29–39 (1999). [https://doi.org/10.1016/S0921-5107\(98\)00440-1](https://doi.org/10.1016/S0921-5107(98)00440-1)
 22. H. Lin, A. Villamor, *Power SiC 2018: materials, devices and applications*. Yole Development (2018). <http://www.yole.fr/>
 23. A. Figueras, S. Garelik, R. Rodríguez-Clemente, B. Armas, C. Combescure, C. Dupuy, A morphological and structural study of SiC layers obtained by LPCVD using tetramethylsilane. *J. Cryst. Growth* **110**, 528–542 (1991). [https://doi.org/10.1016/0022-0248\(91\)90290-L](https://doi.org/10.1016/0022-0248(91)90290-L)
 24. Y.L. Lee, J.M. Sanchez, Simulation of chemical-vapor-deposited silicon carbide for a cold wall vertical reactor. *J. Cryst. Growth* **178**, 505–512 (1997). [https://doi.org/10.1016/S0022-0248\(97\)00090-0](https://doi.org/10.1016/S0022-0248(97)00090-0)
 25. Y.H. Seo, Effects of experimental parameters on void formation in the growth of 3C-SiC thin film on Si substrate. *J. Electrochem. Soc.* **145**, 292 (1998). <https://doi.org/10.1149/1.1838249>
 26. Y. Avigal, M. Schieber, R. Levin, The growth of hetero-epitaxial SiC films by pyrolysis of various alkyl-silicon compounds. *J. Cryst. Growth* **24–25**, 188–192 (1974). [https://doi.org/10.1016/0022-0248\(74\)90302-9](https://doi.org/10.1016/0022-0248(74)90302-9)
 27. A.M. Wrobel, A. Walkiewicz-Pietrzykowska, M. Ahola, I.J. Vayrynen, F.J. Ferrer-Fernandez, A.R. Gonzalez-Elipse, Growth mechanism and chemical structure of amorphous hydrogenated silicon carbide (a-SiC:H) films formed by remote hydrogen microwave plasma CVD from a triethylsilane precursor: part I. *Chem. Vap. Depos.* **15**, 39–46 (2009). <https://doi.org/10.1002/cvde.200806726>
 28. C. Lu, L. Cheng, C. Zhao, L. Zhang, Y. Xu, Kinetics of chemical vapor deposition of SiC from methyltrichlorosilane and hydrogen. *Appl. Surf. Sci.* **255**, 7495–7499 (2009). <https://doi.org/10.1016/j.apsusc.2009.03.069>
 29. S.-M. Jeong, K.-H. Kim, Y.J. Yoon, M.-H. Lee, W.-S. Seo, Thermodynamic approach to the synthesis of silicon carbide using tetramethylsilane as the precursor at high temperature. *J. Cryst. Growth* **357**, 48–52 (2012). <https://doi.org/10.1016/j.jcrysgro.2012.07.034>
 30. S.-M. Jeong, D.-H. Nam, B.G. Kim, J.-Y. Yoon, M.-H. Lee, K.-H. Kim, Y.J. Yoon, W.-S. Seo, Synthesis of α -SiC from tetramethylsilane by chemical vapor deposition at high temperature. *Appl. Phys. Express* **7**, 025501 (2014). <https://doi.org/10.7567/APEX.7.025501>
 31. D.-H. Nam, B.G. Kim, J.-Y. Yoon, M.-H. Lee, W.-S. Seo, S.-M. Jeong, C.-W. Yang, W.-J. Lee, High-temperature chemical vapor deposition for SiC single crystal bulk growth using tetramethylsilane as a precursor. *Cryst. Growth Des.* **14**, 5569–5574 (2014). <https://doi.org/10.1021/cg5008186>
 32. B.G. Kim, J.-Y. Yoon, C.-H. Yoo, D.-H. Nam, M.-H. Lee, W.-S. Seo, S.-M. Jeong, Condensation of vapor species at the outlets in high temperature chemical vapor deposition using tetramethylsilane as a precursor for SiC bulk growth. *CrystEngComm* **17**, 3148–3152 (2015). <https://doi.org/10.1039/C4CE02472A>
 33. J.-Y. Yoon, B. Geun Kim, D.-H. Nam, C.-H. Yoo, M.-H. Lee, W.-S. Seo, Y.-G. Shul, W.-J. Lee, S.-M. Jeong, Design of a high temperature chemical vapor deposition reactor in which the effect of the condensation of exhaust gas in the outlet is minimized using computational modeling. *J. Cryst. Growth* **435**, 84–90 (2016). <https://doi.org/10.1016/j.jcrysgro.2015.11.039>
 34. K.-H. Kim, K.-J. Hwang, H. Lee, S.-M. Jeong, M.-H. Lee, S.-Y. Bae, Improvement of adhesion properties of glass prepared using SiC-deposited graphite mold via low-temperature chemical vapor deposition. *J. Korean Ceram. Soc.* **57**, 112–118 (2020). <https://doi.org/10.1007/s43207-019-00010-2>
 35. T. Ujihara, S. Kozawa, K. Seki, Y. Yamamoto, S. Harada, Conversion mechanism of threading screw dislocation during SiC solution growth. *Mater. Sci. Forum* **717–720**, 351–354 (2012). <https://doi.org/10.4028/www.scientific.net/MSF.717-720.351>
 36. S. Harada, Y. Yamamoto, K. Seki, A. Horio, M. Tagawa, T. Ujihara, Different behavior of threading edge dislocation conversion during the solution growth of 4H-SiC depending on the Burgers vector. *Acta Mater.* **81**, 284–290 (2014). <https://doi.org/10.1016/j.actamat.2014.08.027>
 37. C.D. Stinespring, J.C. Wormhoudt, Gas phase kinetics analysis and implications for silicon carbide chemical vapor deposition. *J. Cryst. Growth* **87**, 481–493 (1988). [https://doi.org/10.1016/0022-0248\(88\)90096-6](https://doi.org/10.1016/0022-0248(88)90096-6)
 38. S. Harada, G. Hatasa, K. Murayama, T. Kato, M. Tagawa, T. Ujihara, Solvent design for high-purity SiC solution growth. *Mater. Sci. Forum* **897**, 32–35 (2017). <https://doi.org/10.4028/www.scientific.net/MSF.897.32>
 39. Q.-S. Chen, H. Zhang, V. Prasad, C.M. Balkas, N.K. Yushin, Modeling of heat transfer and kinetics of physical vapor transport growth of silicon carbide crystals. *J. Heat Transf.* **123**, 1098–1109 (2001). <https://doi.org/10.1115/1.1409263>
 40. S.Y. Karpov, Y.N. Makarov, M.S. Ramm, Simulation of sublimation growth of SiC single crystals. *Phys. Status Solidi B* **202**, 201–220 (1997). [https://doi.org/10.1002/1521-3951\(199707\)202:1%3c201::AID-PSSB201%3e3.0.CO;2-T](https://doi.org/10.1002/1521-3951(199707)202:1%3c201::AID-PSSB201%3e3.0.CO;2-T)
 41. Y.E. Egorov, A.O. Galyukov, S.G. Gurevich, Y.N. Makarov, E.N. Mokhov, M.G. Ramm, M.S. Ramm, A.D. Roenkov, A.S. Segal, Y.A. Vodakov, A.N. Vorob’ev, A.I. Zhmakin, Modeling analysis of temperature field and species transport inside the system for sublimation growth of SiC in tantalum container. *Mater. Sci. Forum* **264–268**, 61–64 (1998). <https://doi.org/10.4028/www.scientific.net/MSF.264-268.61>
 42. M.S. Ramm, E.N. Mokhov, S.E. Demina, M.G. Ramm, A.D. Roenkov, Yu.A. Vodakov, A.S. Segal, A.N. Vorob’ev, S.Y. Karpov, A.V. Kulik, Yu.N. Makarov, Optimization of sublimation growth of SiC bulk crystals using modeling. *Mater. Sci. Eng. B* **61–62**, 107–112 (1999). [https://doi.org/10.1016/S0921-5107\(98\)00456-5](https://doi.org/10.1016/S0921-5107(98)00456-5)

43. M. Selder, L. Kadinski, Yu. Makarov, F. Durst, P. Wellmann, T. Straubinger, D. Hofmann, S. Karpov, M. Ramm, Global numerical simulation of heat and mass transfer for SiC bulk crystal growth by PVT. *J. Cryst. Growth* **211**, 333–338 (2000). [https://doi.org/10.1016/S0022-0248\(99\)00853-2](https://doi.org/10.1016/S0022-0248(99)00853-2)
44. J. Steiner, M. Arzig, A. Denisov, P.J. Wellmann, Impact of varying parameters on the temperature gradients in 100 mm silicon carbide bulk growth in a computer simulation validated by experimental results. *Cryst. Res. Technol.* **55**, 1900121 (2020). <https://doi.org/10.1002/crat.201900121>
45. J.-Y. Yan, Q.-S. Chen, Y.-N. Jiang, H. Zhang, Improvement of the thermal design in the SiC PVT growth process. *J. Cryst. Growth* **385**, 34–37 (2014). <https://doi.org/10.1016/j.jcrysgro.2013.02.031>
46. J. Drowart, G. De Maria, M.G. Inghram, Thermodynamic study of SiC utilizing a mass spectrometer. *J. Chem. Phys.* **29**, 1015–1021 (1958). <https://doi.org/10.1063/1.1744646>
47. S.K. Lilov, Study of the equilibrium processes in the gas phase during silicon carbide sublimation. *Mater. Sci. Eng. B* **21**, 65–69 (1993). [https://doi.org/10.1016/0921-5107\(93\)90267-Q](https://doi.org/10.1016/0921-5107(93)90267-Q)
48. K. Ariyawong, C. Chatillon, E. Blanquet, J.-M. Dedulle, D. Chaussende, A first step toward bridging silicon carbide crystal properties and physical chemistry of crystal growth. *CrystEngComm* **18**, 2119–2124 (2016). <https://doi.org/10.1039/C5CE02480C>
49. B. Gao, X.J. Chen, S. Nakano, S. Nishizawa, K. Kakimoto, Analysis of SiC crystal sublimation growth by fully coupled compressible multi-phase flow simulation. *J. Cryst. Growth* **312**, 3349–3355 (2010). <https://doi.org/10.1016/j.jcrysgro.2010.08.032>
50. D. Nakamura, Simple and quick enhancement of SiC bulk crystal growth using a newly developed crucible material. *Appl. Phys. Express* **9**, 055507 (2016). <https://doi.org/10.7567/APEX.9.055507>
51. D. Hofmann, M. Bickermann, R. Eckstein, M. Kölbl, S.G. Müller, E. Schmitt, A. Weber, A. Winnacker, Sublimation growth of silicon carbide bulk crystals: experimental and theoretical studies on defect formation and growth rate augmentation. *J. Cryst. Growth* **198–199**, 1005–1010 (1999). [https://doi.org/10.1016/S0022-0248\(98\)01212-3](https://doi.org/10.1016/S0022-0248(98)01212-3)
52. H. Das, S. Sunkari, J. Justice, H. Pham, G. Park, Y.H. Seo, Statistical analysis of killer and non-killer defects in SiC and the impacts to device performance. *Mater. Sci. Forum* **1004**, 458–463 (2020). <https://doi.org/10.4028/www.scientific.net/MSF.1004.458>
53. E.Y. Tupitsyn, A. Arulchakkaravarthi, R.V. Drachev, T.S. Sudarshan, Controllable 6H-SiC to 4H-SiC polytype transformation during PVT growth. *J. Cryst. Growth* **299**, 70–76 (2007). <https://doi.org/10.1016/j.jcrysgro.2006.10.258>
54. X. Liu, B. Chen, L.-X. Song, E.-W. Shi, Z.-Z. Chen, The behavior of powder sublimation in the long-term PVT growth of SiC crystals. *J. Cryst. Growth* **312**, 1486–1490 (2010). <https://doi.org/10.1016/j.jcrysgro.2010.01.029>
55. A.V. Kulik, M.V. Bogdanov, SYu. Karpov, M.S. Ramm, Y.N. Makarov, Theoretical analysis of the mass transport in the powder charge in long-term bulk SiC growth. *Mater. Sci. Forum* **457–460**, 67–70 (2004). <https://doi.org/10.4028/www.scientific.net/MSF.457-460.67>
56. R. Ma, H. Zhang, V. Prasad, M. Dudley, Growth kinetics and thermal stress in the sublimation growth of silicon carbide. *Cryst. Growth Des.* **2**, 213–220 (2002). <https://doi.org/10.1021/cg015572p>
57. I.A. Zhmakin, A.V. Kulik, SYu. Karpov, S.E. Demina, M.S. Ramm, Yu.N. Makarov, Evolution of thermoelastic strain and dislocation density during sublimation growth of silicon carbide. *Diam. Relat. Mater.* **9**, 446–451 (2000). [https://doi.org/10.1016/S0925-9635\(99\)00307-6](https://doi.org/10.1016/S0925-9635(99)00307-6)
58. M. Selder, L. Kadinski, F. Durst, T.L. Straubinger, P.J. Wellmann, D. Hofmann, Numerical simulation of thermal stress formation during PVT-growth of SiC bulk crystals. *Mater. Sci. Forum* **353–356**, 65–68 (2001). <https://doi.org/10.4028/www.scientific.net/MSF.353-356.65>
59. E. Schmitt, M. Rasp, A.D. Weber, M. Kölbl, R. Eckstein, L. Kadinski, M. Selder, Defect reduction in sublimation grown silicon carbide crystals by adjustment of thermal boundary conditions. *Mater. Sci. Forum* **353–356**, 15–20 (2001). <https://doi.org/10.4028/www.scientific.net/MSF.353-356.15>
60. A.S. Jordan, R. Caruso, A.R. VonNeida, J.W. Nielsen, A comparative study of thermal stress induced dislocation generation in pulled GaAs, InP, and Si crystals. *J. Appl. Phys.* **52**, 3331–3336 (1981). <https://doi.org/10.1063/1.329154>
61. Y. Kang, C.-H. Yoo, D.-H. Nam, M.-H. Lee, W.-S. Seo, S. Hong, S.-M. Jeong, Thermodynamic design of a high temperature chemical vapor deposition process to synthesize α -SiC in Si-C-H and Si-C-H-Cl systems. *J. Cryst. Growth* **485**, 78–85 (2018). <https://doi.org/10.1016/j.jcrysgro.2018.01.001>
62. Y. Kito, E. Makino, K. Ikeda, M. Nagakubo, S. Onda, SiC HTCVD simulation modified by sublimation etching. *Mater. Sci. Forum* **527–529**, 107–110 (2006). <https://doi.org/10.4028/www.scientific.net/MSF.527-529.107>
63. N. Hoshino, I. Kamata, Y. Tokuda, E. Makino, N. Sugiyama, J. Kojima, H. Tsuchida, High-speed, high-quality crystal growth of 4H-SiC by high-temperature gas source method. *Appl. Phys. Express* **7**, 065502 (2014). <https://doi.org/10.7567/APEX.7.065502>
64. J. Kojima, Y. Tokuda, E. Makino, N. Sugiyama, N. Hoshino, I. Kamata, H. Tsuchida, Developing technologies of SiC gas source growth method. *Mater. Sci. Forum* **858**, 23–28 (2016). <https://doi.org/10.4028/www.scientific.net/MSF.858.23>
65. Y. Tokuda, N. Hoshino, H. Kuno, H. Uehigashi, T. Okamoto, T. Kanda, N. Ohya, I. Kamata, H. Tsuchida, Fast 4H-SiC bulk growth by high-temperature gas source method. *Mater. Sci. Forum* **1004**, 5–13 (2020). <https://doi.org/10.4028/www.scientific.net/MSF.1004.5>
66. Ö. Danielsson, A. Henry, E. Janzén, Growth rate predictions of chemical vapor deposited silicon carbide epitaxial layers. *J. Cryst. Growth* **243**, 170–184 (2002). [https://doi.org/10.1016/S0022-0248\(02\)01486-0](https://doi.org/10.1016/S0022-0248(02)01486-0)
67. J. Kojima, E. Makino, Y. Tokuda, N. Sugiyama, N. Hoshino, H. Tsuchida, High-speed and long-length SiC growth using high-temperature gas source method. *Mater. Sci. Forum* **821–823**, 104–107 (2015). <https://doi.org/10.4028/www.scientific.net/MSF.821-823.104>
68. M.A. Fanton, B.E. Weiland, D.W. Snyder, J.M. Redwing, Thermodynamic equilibrium limitations on the growth of SiC by halide chemical vapor deposition. *J. Appl. Phys.* **101**, 014903 (2007). <https://doi.org/10.1063/1.2399882>
69. Y.N. Makarov, R.A. Talalaev, A.N. Vorob'ev, M.S. Ramm, M.V. Bogdanov, Computational analysis of SiC HTCVD from silicon tetrachloride and propane. *Mater. Sci. Forum* **600–603**, 51–53 (2009). <https://doi.org/10.4028/www.scientific.net/MSF.600-603.51>
70. Y. Kito, E. Makino, K. Inaba, N. Hosokawa, H. Hiramatsu, J. Hasegawa, S. Onda, H. Tsuboi, H. Takaba, A. Miyamoto, Simulation study for HTCVD of SiC using first-principles calculation and thermo-fluid analysis. *Mater. Sci. Forum* **600–603**, 47–50 (2009). <https://doi.org/10.4028/www.scientific.net/MSF.600-603.47>
71. J.-W. Seo, K. Choi, Application of CFD simulation to silicon carbide deposition for nozzles with funnel. *J. Korean*

- Ceram. Soc. **58**, 184–191 (2021). <https://doi.org/10.1007/s43207-020-00082-5>
72. Centre for Research in Computational Thermochemistry, FactSage database documentation (2021). <https://www.crct.polymtl.ca/fact/documentation/>. Accessed 7 Sept 2021
 73. T. Okamoto, T. Kanda, Y. Tokuda, N. Ohya, K. Betsuyaku, N. Hoshino, I. Kamata, H. Tsuchida, Development of 150-mm 4H-SiC substrates using a high-temperature chemical vapor deposition method. *Mater. Sci. Forum* **1004**, 14–19 (2020). <https://doi.org/10.4028/www.scientific.net/MSF.1004.14>
 74. F. Mercier, J.-M. Dedulle, D. Chaussende, M. Pons, Coupled heat transfer and fluid dynamics modeling of high-temperature SiC solution growth. *J. Cryst. Growth* **312**, 155–163 (2010). <https://doi.org/10.1016/j.jcrysgro.2009.10.007>
 75. T. Yamamoto, Y. Okano, T. Ujihara, S. Dost, Global simulation of the induction heating TSSG process of SiC for the effects of Marangoni convection, free surface deformation and seed rotation. *J. Cryst. Growth* **470**, 75–88 (2017). <https://doi.org/10.1016/j.jcrysgro.2017.04.016>
 76. M.-T. Ha, Y.-J. Yu, Y.-J. Shin, S.-Y. Bae, M.-H. Lee, C.-J. Kim, S.-M. Jeong, Flow modification enhancing the growth rate in top seeded solution growth of SiC crystals. *RSC Adv.* **9**, 26327–26337 (2019). <https://doi.org/10.1039/C9RA04930D>
 77. K. Ariyawong, J.M. Dedulle, D. Chaussende, Electromagnetic enhancement of carbon transport in SiC solution growth process: a numerical modeling approach. *Mater. Sci. Forum* **778–780**, 71–74 (2014). <https://doi.org/10.4028/www.scientific.net/MSF.778-780.71>
 78. F. Mercier, S. Nishizawa, Solution growth of SiC from silicon melts: Influence of the alternative magnetic field on fluid dynamics. *J. Cryst. Growth* **318**, 385–388 (2011). <https://doi.org/10.1016/j.jcrysgro.2010.10.022>
 79. T. Yamamoto, N. Adkar, Y. Okano, T. Ujihara, S. Dost, Numerical investigation of the transport phenomena occurring in the growth of SiC by the induction heating TSSG method. *J. Cryst. Growth* **474**, 50–54 (2017). <https://doi.org/10.1016/j.jcrysgro.2016.12.086>
 80. L. Wang, T. Horiuchi, A. Sekimoto, Y. Okano, T. Ujihara, S. Dost, Three-dimensional numerical analysis of Marangoni convection occurring during the growth process of SiC by the RF-TSSG method. *J. Cryst. Growth* **520**, 72–81 (2019). <https://doi.org/10.1016/j.jcrysgro.2019.05.017>
 81. J. Lefebure, J.-M. Dedulle, T. Ouisse, D. Chaussende, Modeling of the growth rate during top seeded solution growth of SiC using pure silicon as a solvent. *Cryst. Growth Des.* **12**, 909–913 (2012). <https://doi.org/10.1021/cg201343w>
 82. T. Narumi, S. Kawanishi, T. Yoshikawa, K. Kusunoki, K. Kamei, H. Daikoku, H. Sakamoto, Thermodynamic evaluation of the C–Cr–Si, C–Ti–Si, and C–Fe–Si systems for rapid solution growth of SiC. *J. Cryst. Growth* **408**, 25–31 (2014). <https://doi.org/10.1016/j.jcrysgro.2014.08.027>
 83. S. Kawanishi, Y. Nagamatsu, T. Yoshikawa, H. Shibata, Availability of Cr-rich Cr-Si solvent for rapid solution growth of 4H-SiC. *J. Cryst. Growth* **549**, 125877 (2020). <https://doi.org/10.1016/j.jcrysgro.2020.125877>
 84. J.E. Lee, B.G. Kim, J.-Y. Yoon, M.-T. Ha, M.-H. Lee, Y. Kim, W.-S. Seo, H.-J. Choi, W.-J. Lee, S.-M. Jeong, The role of an SiC interlayer at a graphite–silicon liquid interface in the solution growth of SiC crystals. *Ceram. Int.* **42**, 11611–11618 (2016). <https://doi.org/10.1016/j.ceramint.2016.04.060>
 85. S.H. Choi, Y.G. Kim, Y.J. Shin, S.M. Jeong, M.H. Lee, C.Y. Lee, J.M. Choi, M.S. Park, Y.S. Jang, W.J. Lee, The effect of stepped wall of the graphite crucible in top seeded solution growth of SiC crystal. *Mater. Sci. Forum* **924**, 27–30 (2018). <https://doi.org/10.4028/www.scientific.net/MSF.924.27>
 86. M.-T. Ha, Y.-J. Shin, M.-H. Lee, C.-J. Kim, S.-M. Jeong, Effects of the temperature gradient near the crystal–melt interface in top seeded solution growth of SiC crystal. *Phys. Status Solidi A* **215**, 1701017 (2018). <https://doi.org/10.1002/pssa.201701017>
 87. M.-T. Ha, Y.-J. Shin, S.-Y. Bae, S.-Y. Park, S.-M. Jeong, Effect of hot-zone aperture on the growth behavior of SiC single crystal produced via top-seeded solution growth method. *J. Korean Ceram. Soc.* **56**, 589–595 (2019). <https://doi.org/10.4191/kcers.2019.56.6.07>
 88. T.-Y. Park, Y.-J. Shin, M.-T. Ha, S.-Y. Bae, Y.-S. Lim, S.-M. Jeong, Effect of radiation heat transfer on the control of temperature gradient in the induction heating furnace for growing single crystals. *J. Korean Inst. Electr. Electron. Mater. Eng.* **32**, 522–527 (2019). <https://doi.org/10.4313/JKEM.2019.32.6.522>
 89. Y.G. Kim, S.H. Choi, Y.J. Shin, S.M. Jeong, M.H. Lee, C.Y. Lee, J.M. Choi, M.S. Park, Y.S. Jang, W.J. Lee, Modification of crucible shape in top seeded solution growth of SiC crystal. *Mater. Sci. Forum* **924**, 47–50 (2018). <https://doi.org/10.4028/www.scientific.net/MSF.924.47>
 90. B. Liu, Y. Yu, X. Tang, B. Gao, Optimization of crucible and heating model for large-sized silicon carbide ingot growth in top-seeded solution growth. *J. Cryst. Growth* **533**, 125406 (2020). <https://doi.org/10.1016/j.jcrysgro.2019.125406>
 91. K. Fujii, K. Takei, M. Aoshima, N. Senguttuvan, M. Hiratani, T. Ujihara, Y. Matsumoto, T. Kato, K. Kurashige, H. Okumura, Influences of solution flow and lateral temperature distribution on surface morphology in solution growth of SiC. *Mater. Sci. Forum* **821–823**, 35–38 (2015). <https://doi.org/10.4028/www.scientific.net/MSF.821-823.35>
 92. K. Kusunoki, K. Kamei, N. Okada, K. Moriguchi, H. Kaido, H. Daikoku, M. Kado, K. Danno, H. Sakamoto, T. Bessho, T. Ujihara, Top-seeded solution growth of 3 inch diameter 4H-SiC bulk crystal using metal solvents. *Mater. Sci. Forum* **778–780**, 79–82 (2014). <https://doi.org/10.4028/www.scientific.net/MSF.778-780.79>
 93. H. Daikoku, M. Kado, A. Seki, K. Sato, T. Bessho, K. Kusunoki, H. Kaidou, Y. Kishida, K. Moriguchi, K. Kamei, Solution growth on concave surface of 4H-SiC crystal. *Cryst. Growth Des.* **16**, 1256–1260 (2016). <https://doi.org/10.1021/acs.cgd.5b01265>
 94. T. Umezaki, D. Koike, S. Harada, T. Ujihara, Analysis of the carbon transport near the growth interface with respect to the rotational speed of the seed crystal during top-seeded solution growth of SiC. *Jpn. J. Appl. Phys.* **55**, 125601 (2016). <https://doi.org/10.7567/JJAP.55.125601>
 95. K. Kusunoki, K. Kamei, N. Okada, N. Yashiro, A. Yauchi, T. Ujihara, K. Nakajima, Solution growth of SiC crystal with high growth rate using accelerated crucible rotation technique. *Mater. Sci. Forum* **527–529**, 119–122 (2006). <https://doi.org/10.4028/www.scientific.net/MSF.527-529.119>
 96. K. Kurashige, M. Aoshima, K. Takei, K. Fujii, M. Hiratani, N. Senguttuvan, T. Kato, T. Ujihara, Y. Matsumoto, H. Okumura, Effect of forced convection by crucible design in solution growth of SiC single crystal. *Mater. Sci. Forum* **821–823**, 22–25 (2015). <https://doi.org/10.4028/www.scientific.net/MSF.821-823.22>
 97. T. Horiuchi, L. Wang, A. Sekimoto, Y. Okano, T. Yamamoto, T. Ujihara, S. Dost, The effect of crucible rotation and crucible size in top-seeded solution growth of single-crystal silicon carbide. *Cryst. Res. Technol.* **54**, 1900014 (2019). <https://doi.org/10.1002/crat.201900014>
 98. K. Ariyawong, Y.J. Shin, J.-M. Dedulle, D. Chaussende, Analysis of macrostep formation during top seeded solution growth of 4H-SiC. *Cryst. Growth Des.* **16**, 3231–3236 (2016). <https://doi.org/10.1021/acs.cgd.6b00155>
 99. C. Zhu, S. Harada, K. Seki, H. Zhang, H. Niinomi, M. Tagawa, T. Ujihara, Influence of solution flow on step bunching in solution

- growth of SiC crystals. *Cryst. Growth Des.* **13**, 3691–3696 (2013). <https://doi.org/10.1021/cg400706u>
100. T. Umezaki, D. Koike, S. Harada, T. Ujihara, Improvement of surface morphology by solution flow control in solution growth of SiC on off-axis seeds. *Mater. Sci. Forum* **821–823**, 31–34 (2015). <https://doi.org/10.4028/www.scientific.net/MSF.821-823.31>
101. L. Wang, T. Horiuchi, A. Sekimoto, Y. Okano, T. Ujihara, S. Dost, Numerical investigation of the effect of static magnetic field on the TSSG growth of SiC. *J. Cryst. Growth* **498**, 140–147 (2018). <https://doi.org/10.1016/j.jcrysgro.2018.06.017>
102. M.-T. Ha, L.V. Lich, Y.-J. Shin, S.-Y. Bae, M.-H. Lee, S.-M. Jeong, Improvement of SiC crystal growth rate and uniformity via top-seeded solution growth under external static magnetic field: a numerical investigation. *Materials* **13**, 651 (2020). <https://doi.org/10.3390/ma13030651>
103. M.-T. Ha, Y.-J. Shin, S.-Y. Bae, Y.-J. Yoo, S.-M. Jeong, Effect of residual droplet on the solution-grown SiC single crystals. *J. Korean Inst. Electr. Electron. Mater. Eng.* **32**, 516–521 (2019). <https://doi.org/10.4313/JKEM.2019.32.6.516>
104. Y. Tsunooka, N. Kokubo, G. Hatasa, S. Harada, M. Tagawa, T. Ujihara, High-speed prediction of computational fluid dynamics simulation in crystal growth. *CrystEngComm* **20**, 6546–6550 (2018). <https://doi.org/10.1039/C8CE00977E>
105. L. Wang, A. Sekimoto, Y. Takehara, Y. Okano, T. Ujihara, S. Dost, Optimal control of SiC crystal growth in the RF-TSSG system using reinforcement learning. *Curr. Comput.-Aided Drug Des.* **10**, 791 (2020). <https://doi.org/10.3390/cryst10090791>
106. T. Horiuchi, L. Wang, A. Sekimoto, Y. Okano, T. Ujihara, S. Dost, Adjoint-based sensitivity analysis for the optimal crucible temperature profile in the RF-Heating TSSG-SiC crystal growth process. *J. Cryst. Growth* **517**, 59–63 (2019). <https://doi.org/10.1016/j.jcrysgro.2019.04.001>
107. Y. Takehara, A. Sekimoto, Y. Okano, T. Ujihara, S. Dost, Bayesian optimization for a high- and uniform-crystal growth rate in the top-seeded solution growth process of silicon carbide under applied magnetic field and seed rotation. *J. Cryst. Growth* **532**, 125437 (2020). <https://doi.org/10.1016/j.jcrysgro.2019.125437>
108. Y. Takehara, A. Sekimoto, Y. Okano, T. Ujihara, S. Dost, Explainable machine learning for the analysis of transport phenomena in top-seeded solution growth. *J. Therm. Sci. Technol.* **16**, JTST0009 (2021). <https://doi.org/10.1299/jtst.2021jtst0009>
109. W. Yu, C. Zhu, Y. Tsunooka, W. Huang, Y. Dang, K. Kutsukake, S. Harada, M. Tagawa, T. Ujihara, Geometrical design of a crystal growth system guided by a machine learning algorithm. *CrystEngComm* **23**, 2695–2702 (2021). <https://doi.org/10.1039/D1CE00106J>
110. Y. Mukaiyama, M. Iizuka, A. Vorobev, V. Kalaev, Numerical investigation of the effect of shape change in graphite crucible during top-seeded solution growth of SiC. *J. Cryst. Growth* **475**, 178–185 (2017). <https://doi.org/10.1016/j.jcrysgro.2017.06.006>
111. Y. Dang, C. Zhu, M. Ikumi, M. Takaishi, W. Yu, W. Huang, X. Liu, K. Kutsukake, S. Harada, M. Tagawa, T. Ujihara, Adaptive process control for crystal growth using machine learning for high-speed prediction: an application to SiC solution growth. *CrystEngComm* (2021). <https://doi.org/10.1039/D0CE01824D>

Publisher's Note Springer Nature remains neutral with regard to jurisdictional claims in published maps and institutional affiliations.